Elucidation of the activity and pH stability limits of polyoxometalate-intercalated layered double hydroxide nanocomposites towards water oxidation catalysis

Joaquín Soriano-López,[a]* Javier Quirós-Huerta,[a] Álvaro Seijas-Da Silva,[a] Ramón Torres-Cavanillas,[a] Eduardo Andres-Garcia,[a] Gonzalo Abellán[a] and Eugenio Coronado[a]

[a]Institut de Ciència Molecular, Universitat de València, Catedrático José Beltrán 2, 46980 Paterna, Spain

*Correspondence to: joaquin.soriano@uv.es

ABSTRACT

The inclusion of water oxidation active polyoxometalates (POMs) inside layered materials is a promising strategy to increase their catalytic efficiency while overcoming their fragility under homogeneous conditions. In this sense, intercalation of POMs in the interlaminar space of layered double hydroxides (LDHs), formed by positively charged brucite-type inorganic layers, is a very interesting strategy that is gaining attention in the field. Despite their huge potential, there is a lack of accurate characterization of the materials, especially after their use as water oxidation catalysts in pH conditions in which the POM counterpart has been demonstrated to be unstable (strong alkali media). For this reason and as a proof-of-concept, we have intercalated the well-known $[Co_4(H_2O)_2(PW_9O_{34})_2]^{10-}$ POM (**Co₄-POM**) in the lamellar space of the **Mg₂Al-LDH** layered double hydroxide, to study its catalytical capabilities and stability. Remarkably, the nanocomposites show improved water oxidation efficiencies with excellent stability in close-to-neutral media compared to the water-insoluble cesium salt of **Co₄-POM** or commercial Co_3O_4. However, thorough post-catalytic characterization of the nanocomposites demonstrates that the polyoxotungstate framework of the POM suffers from hydrolytic instability in strong alkali conditions, leading to the formation of a mixed-valence cobalt(II/III) oxide in the interlayer space of **Mg₂Al-LDH**. This work highlights the importance of accurately assessing the fate of the catalytical POM after the catalytic reaction, especially when employing conditions outside the pH stability window of the POM, which can lead to erroneous conclusions and mistaken catalytic activities.

Keywords: Electrocatalytic water oxidation, polyoxometalates, layered double hydroxides, composite nanomaterials, hybrid nanomaterials, materials characterization.

INTRODUCTION

Climate change and global warming caused by the use of fossil fuels to produce energy urges us to rapidly change the energy production paradigm to environmentally friendly, efficient, and cost-effective alternatives.[1,2] Hydrogen has the potential to contribute to this goal as the energy vector in a carbon-free energy system.[3] The baseline technology for green hydrogen production is water electrolysis, which uses as inputs electricity powered from renewable resources and pure water to produce hydrogen and oxygen through the water splitting reaction.[4] In this scheme, the water oxidation semi-reaction, also known as the Oxygen Evolution Reaction (OER), represents the bottleneck for the development of new technologies and energy storage concepts.[5] This is due to its high thermodynamic requirements and sluggish kinetics, which typically require the use of scarce and geolocated elements that drastically limit the wide deployment of novel energy technologies.[6] Therefore, there is an urgent need to develop and optimize new OER nanomaterials based on earth-abundant elements for achieving sustainable hydrogen production via electrolysis.[7]

The OER capabilities of transition-metal-substituted polyoxometalates (POMs) have been studied during the last years since they offer high stability under strong oxidizing conditions and rich intrinsic redox chemistry.[8] Particularly interesting are Cobalt-substituted POMs (Co-POMs), which are nowadays known to be genuine robust molecular OER electrocatalysts displaying excellent activities.[9–11] Thanks to their high chemical amenability it was possible to study structure-reactivity relationships that contributed to pinpoint the contribution of each of the different moieties that compose their structures.[12–18] Nevertheless, water electrolysis technologies require the immobilization of the molecular Co-POM into solid supports resulting in hybrid catalysts working in the solid-state, which in turn can increase the stability and OER efficiency of the molecular counterpart.[19] Different strategies have been used in this area focused on the electrostatic interaction between the negatively charged Co-POM and positively charged 3-dimensional supports, for instance, mesoporous carbon nitride or zeolitic imidazolate frameworks.[20,21] In this respect, layered materials such as layered double hydroxides (LDHs) can play a crucial role in the immobilization of Co-POMs since they provide positively charged surfaces in between the layers that can accommodate the Co-POMs to form self-assembled POM/LDH nanocomposites via established electrostatic and hydrogen bond interactions.[22,23] The laminar nature of the LDH provides additional advantages for the Co-POMs heterogenization since they result in OER nanomaterials with high surface area and good mechanical strength and chemical stability, as well as an enhancement of charge separation by minimizing the path channels in which electrons have to migrate during the electrocatalytic reaction.[24] Importantly, the confinement effect created at the LDH interlayer space prevents the leaching of the POM species into the reaction media, thus overcoming one of the biggest drawbacks of electrostatically supporting POMs on 3D and 2D surfaces.[25]

Therefore, the synergistic effects that appear at the POM/LDH interface can boost the stability and catalytic activity of the hybrid nanomaterials compared to their constituents separately. This characteristic has made POM/LDH nanocomposites very attractive nanomaterials for diverse catalytic reactions. For instance, Song and co-workers reported the intercalation of a Zn-substituted Dawson-type POM (ZnP_2W_{17}) into a Mg_3Al-suberic LDH precursor leading to the formation of the ZnP_2W_{17}/Mg_3Al hybrid, which showed superior catalytic efficiency and selectivity towards the sulfoxidation of various sulfides compared to that of the POM or LDH precursors separately.[26] Miras and colleagues prepared a POM/LDH hybrid containing the Zn_4-Weakley sandwich POM and the Mg_2Al-Tris LDH (Tris = Tris(hydroxymethyl)aminomethane). The

Zn_4/Mg_2Al nanocomposite demonstrated efficient bifunctional catalysis for cascade reactions involving the oxidation of benzyl alcohol to benzaldehyde promoted by the POM species in the presence of H_2O_2. The reaction then occurs through a Knoevenagel condensation step between the benzaldehyde and ethyl cyanoacetate at the basic sites of the LDH counterpart, which lead to the production of benzylidene ethyl cyanoacetate with excellent activity and selectivity.[27] Surprisingly, the use of POM/LDH nanocomposites as OER materials is far less explored, whereby only few examples can be found in literature. Wang a co-workers intercalated the OER inactive Keggin-type POM $[PW_{12}O_{40}]^{3-}$ into a Ni_2Fe-LDH to boost its OER performance.[28] This POM/LDH nanocomposite showed superior OER performance under strong basic conditions than the bare Ni_2Fe-LDH. However, postcatalytic characterization of the compound is highly required in order to clearly address the role and fate of the Keggin POM during turnover conditions, since it is well known that the Keggin anion is only stable below pH 2, it forms lacunary species at pH values between 2 and 9, and it completely dissolves above pH 9.[29] Yu and Liang intercalated different transition metal monosubstituted Keggin POMs into MgAl-Tris LDH.[30] OER electrocatalytic tests showed that the hybrid bearing the Co-POM showed good electrocatalytic properties at neutral pH values, whereas post-catalytic characterization of the recovered materials suggests that the Co-POM maintained its structure during the water oxidation reaction with most of the initial Co(II) ions appearing in higher oxidation states, most likely as Co(III) ions. Interestingly, authors demonstrated that carrying out the experiments at pH 10 leads to deactivation of the hybrid nanomaterial due to the poor hydrolytic stability of this Co-POM at the mentioned pH. The Tris ligand though, bearing three primary alcohols, can be easily oxidized under the strong oxidative environment created during the OER measurements, which will mask the real current density assigned to OER.[31,32] Therefore, quantification of the oxygen evolved in these experiments would be very interesting to clarify the Faradaic efficiency of the system. More recently, Ni and co-workers reported the bifunctional electrocatalytic activity for OER and HER of a hybrid POM/LDH system composed by the phospho-molybdate Wells-Dawson type POM (P_2Mo_{18}) and the ZnFe-LDH directly formed on a Nickel foam electrode.[33] Again, the role and fate of the POM need to be carefully assessed in these structures since it is well known that P_2Mo_{18} possesses a very low hydrolytic stability in solution regardless of the pH of the media.[34,35] Hence, it would not be surprising that the POM structure is not maintained during the electrocatalytic tests performed in strong alkali media. This highlights the importance of selecting the proper working conditions that allow us to define the boundaries of action of the electroactive material and to study in detail the synergies that appear at the molecular/2D material interface. This knowledge will be pivotal for the rational design of novel hybrid nanomaterials with improved catalytic capabilities and durability.

In this work, we report the preparation of **Co_4/Mg_2Al** nanocomposites through the intercalation of the OER active POM $[Co_4(H_2O)_2(PW_9O_{34})_2]^{10-}$ (**Co_4-POM**) in the lamellar space of a Mg_2Al LDH (**Mg_2Al-LDH**) (Scheme 1). Employing different reaction conditions allowed us to obtain the nanocomposites with increasing amounts of the intercalated POM. These **Co_4/Mg_2Al** nanocomposites were tested as OER materials in different working conditions, from neutral to strong alkali media. Our electrocatalytic results show that the OER activity does not scale with the quantity of **Co_4-POM** present in the materials, hence permitting to optimize the OER efficiency of the system by employing just the required amount of POM. Different ex-situ and in-situ characterization methods performed on the **Co_4/Mg_2Al** nanocomposites demonstrate the fate of the **Co_4-POM** as part of the nanocomposites in the different reaction conditions. We clearly observe that the **Co_4-POM** is not stable under strong basic conditions, where Co(II) ions are expelled from the POM framework leading to the **Mg_2Al-LDH** with Co(II) ions present in the

3

lamellar space, which are partially oxidized to Co(III) under the OER applied potential. It is interesting to mention that in the later scenario, the W and P atoms conforming the POM are lost almost completely from the hybrids. On the other hand, the material is stable in neutral media, while a possible partial decomposition of **Co₄-POM** occurs at pH 9 where **Co₄-POM** and related species may coexist in the hybrids during OER conditions.

RESULTS

For this study we have selected the **Mg₂Al-LDH** for the intercalation of **Co₄-POM** for different reasons: (i) it is one of the most studied LDHs and its synthetic protocols as well as its properties are well studied; (ii) platelet-like microcrystals with well-defined hexagonal shape and with large, homogeneous sizes can be obtained using the urea hydrolysis method that will allow for a more facile characterization of the POM/LDH nanocomposites; and (iii) **Mg₂Al-LDH** does not contain catalytically active metal sites and therefore, we can safely assume that the OER activity observed by the nanocomposites arises just from the POM counterpart. Therefore, we synthesized the **Mg₂Al-LDH** following the urea hydrolysis method under hydrothermal conditions,[36] which yielded hexagonal platelet-like microcrystals of ca. 2 µm in diameter (Figure S3). This synthetic method typically yields carbonate intercalated LDHs, as it was confirmed by FTIR spectroscopy (Figure S2), and due to the high affinity of LDHs to carbonate, which may preclude the proper intercalation of POMs, it had to be exchanged by chloride anions. This anion exchange was carried out by dispersing the **Mg₂Al-LDH** in a 1 M NaCl aqueous solution containing HCl 3.3 mM.[37] Note that this step was performed at least twice to ensure the proper removal of the carbonate from the lamellar space. Thereafter, a second anion exchange was performed to prepare three different **Co₄/Mg₂Al** nanocomposites by dispersing the LDH in water for 20 and 60 minutes —samples **Co₄/Mg₂Al_1** and **Co₄/Mg₂Al_2**, respectively—, or in formamide —sample **Co₄/Mg₂Al_3**— followed by the drop-wise addition of an aqueous solution of **Co₄-POM** (see Supplementary Information for more details).
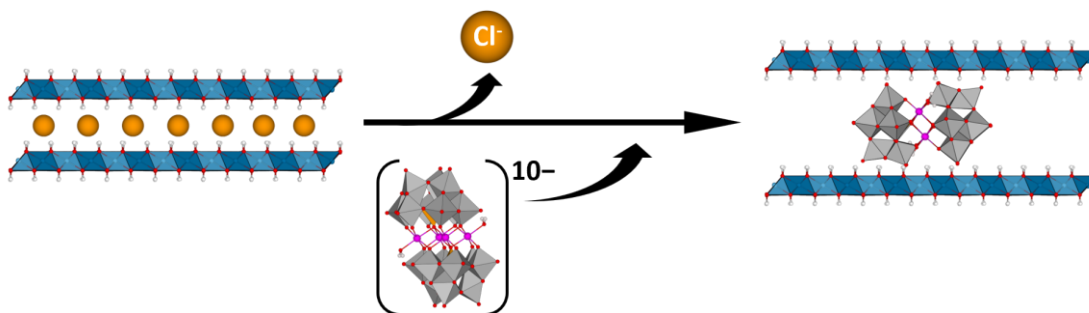
Scheme 1: Schematic representation of the anion exchange process for the obtention of the **Co₄/Mg₂Al** nanocomposites.

Characterization of the **Co₄/Mg₂Al** nanocomposites confirms the successful intercalation of the POM in the lamellar space of the LDH**.** The PXRD pattern of pristine **Mg₂Al-LDH** displays the main basal reflections expected for a hydrotalcite-like material, whereby the position of the (003) and (006) peaks depend on the size of the interlayer anion (Figure 1a). The (003) peak, which is attributed to interlayer reflections, appears at a 2θ value of 11.54°. This corresponds to a basal space distance (d_{BS}) of 7.67 Å; considering a layer thickness of 4.8 Å,[38] the interlayer space distance is 2.87 Å. In the case of the **Co₄/Mg₂Al** nanocomposites the (003) peak is shifted to lower values leading to an increased basal space of 16.67 Å, which corresponds to a lamellar space distance of 11.87 Å. This value is in good agreement with the diameter of the short axis of this Weakley sandwich-type POM (with dimensions of 1.0-1.5 nm),[39] and confirms that the **Co₄-**

4

POM has been intercalated into the interlayer space of the **Mg$_2$Al-LDH** with the C$_{2h}$ symmetrical axis parallel to the host layers. Moreover, this orientation favors the hydrogen-bonding interactions between the hydroxyl groups of the LDH layer and the terminal oxygen atoms on the POM structure. Comparing the PXRD patterns of the three different **Co$_4$/Mg$_2$Al** hybrids we can see that the (003) peak of the pristine **Mg$_2$Al-LDH** is still present for the intercalations performed in water (**Co$_4$/Mg$_2$Al_1** and **Co$_4$/Mg$_2$Al_2**), suggesting only a partial anion exchange in these samples. Moreover, this peak has slightly shifted to 11.45°, which corresponds to a gallery height of 7.74 Å and may indicate the presence of carbonate anions adsorbed during the anion exchange reaction. Therefore, these samples alternate layers intercalated with POM with layers intercalated with chloride and carbonate in the nanocomposite. On the contrary, PXRD of **Co$_4$/Mg$_2$Al_3** only shows a small shoulder of the (003) peak of the pristine LDH at somewhat lower values (10.7 Å), indicating a higher ability of the formamide to exfoliate the LDH slabs resulting in a more successful anion exchange reaction.

Figure S4 shows the FT-IR spectrum of pristine **Co$_4$-POM** displaying peaks at 934, 877, 753 and 697 cm^{-1}, which can be assigned to the vibrations of W-Ot, W-Oc-W, and W-Oe-W (t, terminal; c, corner-sharing; e, edge-sharing), respectively. In the case of the **Co$_4$/Mg$_2$Al** nanocomposites, the W-Ot and W-Oc-W bands appear slightly red-shifted as the result of the electrostatic interaction and hydrogen bonds formed between the POM framework and the LDH layers. Interestingly, those bands associated with the P-O vibrations of the POM heteroatom at ca. 1032 cm^{-1} do not show any shift after the POM intercalation, thus indicating that the interaction of the POM with the LDH occurs purely through the W addenda atoms. The FT-IR spectrum of the pristine **Mg$_2$Al-LDH** shows absorption bands in the 350–800 cm^{-1} range assigned to O-M-O vibrations of the hydrotalcite-like layers of the LDH. These bands also appear shifted in the POM-LDH samples, again indicating an interaction between the POM and the LDH structure and overlap with the W-Oe-W vibrations of the POM framework. Finally, the band appearing at ca. 1360 cm^{-1} in the **Co$_4$/Mg$_2$Al** nanocomposites indicates the presence of carbonate anions that may have been incorporated during the POM intercalation step.

The elemental composition of the **Co$_4$/Mg$_2$Al** nanocomposites and that of the corresponding isolated components were analyzed by ICP-MS (Table S1). The expected Mg:Al ratio of 2:1 is maintained for all the samples, although **Co$_4$/Mg$_2$Al_3** showed a slightly higher concentration of Al(III) ions. This may be caused by the loss of a minimal amount of Mg(II) ions from the LDH structure when dispersing it in formamide. Nevertheless, this did not affect the morphology of the resulting hybrids. On the other hand, we observed in some samples a slightly higher Co ions concentration than the expected values. We ascribe this to an intrinsic artefact of the measurement, since during the digestion process in acid a small portion of the dissolved W(VI) ions may precipitate to form WO$_3$, thus leading to an increase of the Co:W, and P:W ratios. The ICP-MS results allowed us to calculate the amount of **Co$_4$-POM** that has been intercalated in the **Mg$_2$Al-LDH** employing three different methods. As expected, the quantity of **Co$_4$-POM** present in each nanocomposite increases as **Co$_4$/Mg$_2$Al_1** < **Co$_4$/Mg$_2$Al_2** < **Co$_4$/Mg$_2$Al_3**, with calculated LDH:POM ratios of [Mg$_{0.66}$Al$_{0.34}$(OH)$_2$]:[(Co$_4$)$_{0.07}$], [Mg$_{0.67}$Al$_{0.33}$(OH)$_2$]:[(Co$_4$)$_{0.12}$], and [Mg$_{0.64}$Al$_{0.36}$(OH)$_2$]:[(Co$_4$)$_{0.46}$], respectively.

The morphology of the samples was examined with transmission electron microscopy (TEM) images. Figure 1b shows that the initial hexagonal shape of the pristine **Mg$_2$Al-LDH** is retained after the POM intercalation. Note that we could also find partially broken hexagonal crystals produced during the sonication of the LDH to obtain the swollen phase. Additionally, electron diffraction patterns indicate that the high crystallinity of the LDH is partially lost in the hybrid
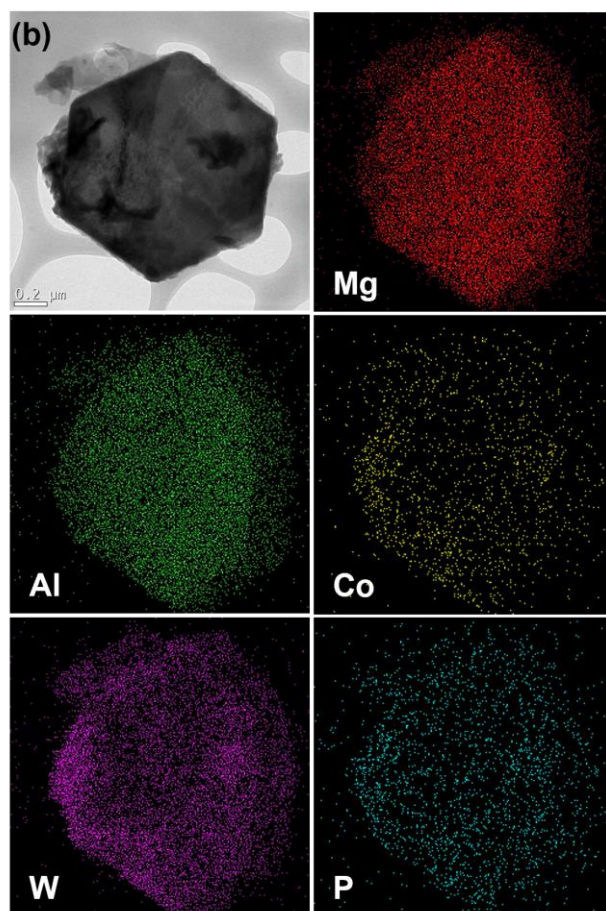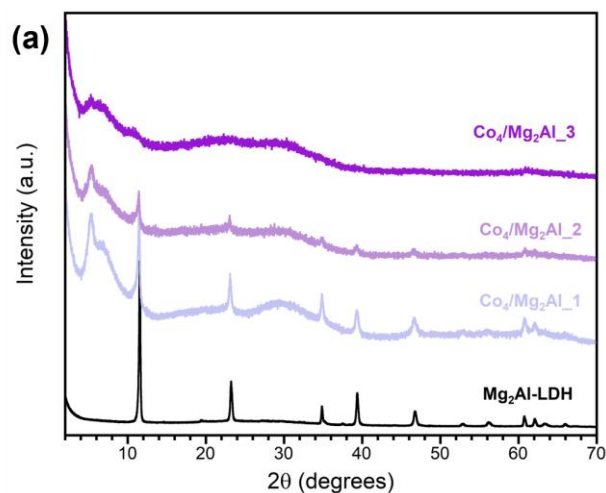
5

nanomaterials (Figure S3), as already observed in the PXRD patterns since restacking of the slabs from the swollen phase does not lead to perfectly aligned layers, showing a pronounced turbostratic disorder. In addition, EDX mapping of the **Co$_4$/Mg$_2$Al_3** sample confirms the presence of all the expected elements and indicates that the **Co$_4$-POM** is well dispersed across the lamellar space of the LDH, Figure 1b.

The successful intercalation was also confirmed by adsorption/desorption isotherm measurements (carbon dioxide; 273 K), where the hybrid nanomaterials show an increased specific surface area with respect to the LDH alone (Figure S5). The presence of POMs evidences a better separation between layers, promoting CO_2 adsorption in the layered material. Moreover, one can clearly see that the hybrids obtained with the formamide method resulted in substantially higher enhancement of the specific surface area compared with that obtained with the water method. Although POM content can be calculated, analyzing its distribution along the layers can be a milestone to understand its application potential: a high %POM can derive in steric impediments, hindering the accessibility to the nanomaterial.

The thermal stability of the samples was unveiled by thermogravimetric differential thermal analysis (TG-DTA) in the 25–700 °C range. Figure S6 shows the TG-DTA of **Mg$_2$Al-LDH** in air in which the first weight loss that can be ascribed to the loss of water molecules. This occurs in two steps that are assigned to the loss of

Figure 1: (a) Powder X-ray diffraction patterns of the hybrid **Co$_4$/Mg$_2$Al** nanocomposites compared to that of the **Mg$_2$Al-LDH**; **(b)** TEM and EDX analysis of the hybrid **Co$_4$/Mg$_2$Al_3** nanocomposite.

surface water molecules at 50–100 °C and the loss of interlayer water molecules at 100–150 °C. The material is stable up to 300 °C where it is then dehydroxylated at 300–395 °C and losses the chloride anions at 395–480 °C. Thereafter, the LDH collapses into an amorphous mixed oxide.
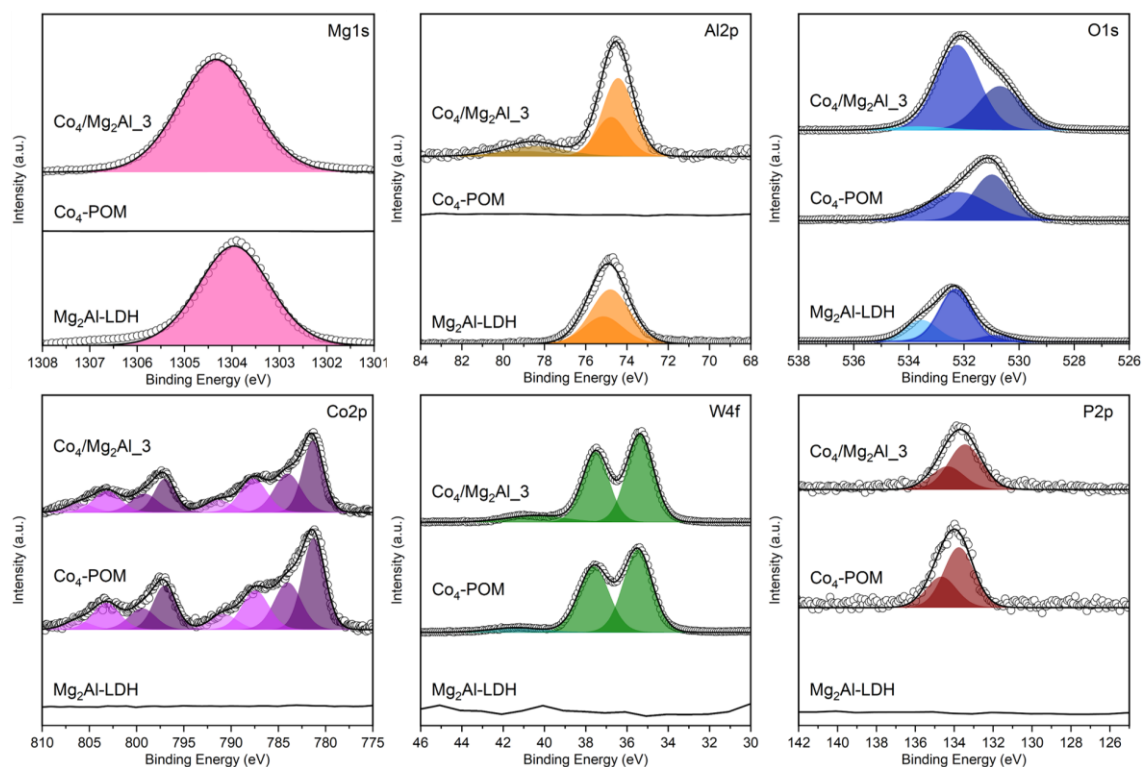
Figure 2: XPS data of the as-synthesized **Mg₂Al-LDH**, **Co₄-POM**, and **Co₄/Mg₂Al_3** samples.

TG-DTA of the POM-LDH samples prepared in water is somehow similar to that of **Mg₂Al-LDH**, although we can find some meaningful differences. The release of surface and interlayer water molecules is slightly slower and occurs up to 250 °C. The dehydroxylation of **Co₄/Mg₂Al_1** and the **Co₄/Mg₂Al_2** occurs in the 300–385 °C range. Finally, the fourth weight loss associated with the loss of chlorine anions is smaller than in the pristine **Mg₂Al-LDH** since most of them have been replaced by **Co₄-POM**. It is interesting to mention that **Co₄/Mg₂Al_2** has a higher total weight loss than **Co₄/Mg₂Al_1**. Looking closely at the TG analysis, we can observe that the main difference in the weight loss compared to **Co₄/Mg₂Al_1** arises from the fourth step. This is contrary to expected given that **Co₄/Mg₂Al_2** has a higher amount of POM molecules. However, the elemental analysis indicates that this sample also has a higher amount of chlorine anions that will account for a higher mass loss before the structure collapses. Following our analysis, we can see that for **Co₄/Mg₂Al_3** the loss of surface and interlamellar water molecules behaves similarly to the hybrids prepared in water. However, an extra weight loss step can be observed between 205–245 °C. The latter can be assigned to the degradation of formamide molecules present in the interlayer space that are trapped during the anion exchange reaction. In addition, the dehydroxylation seems to occur in two different stages, the first one occurring in the 290–335 °C range, which has been previously assigned to the Al-OH dehydroxylation, followed by a second step between 335–390 °C attributed to the simultaneous Mg-OH dehydroxylation and decarbonation.[40]

Figure 2 shows the comparison of the XPS data of the freshly-made materials. Note that only the data corresponding to **Co₄/Mg₂Al_3** is shown. The same Co2p, W4f, and P2P bands can be seen in the hybrid, further supporting that the **Co₄-POM** has been successfully incorporated into the lamellar space of the **Mg₂Al-LDH**. Interestingly, the appearance of a new band in the Al edge of the **Co₄/Mg₂Al_3** nanocomposite suggests that the presence of the **Co₄-POM** may modify the electronic structure of Al in the LDH. In fact, this behavior is not surprising since one would expect a stronger interaction of the **Co₄-POM** with the trivalent Al ions in the LDH since these

7

are the metals that carry the positive charge in the LDH layer. In addition, we observe in the O1s edge of the **Co₄/Mg₂Al_3** nanocomposite the increase in the intensity of terminal M-O species compared to that of **Mg₂Al-LDH**, which can be assigned to the terminal W=O moieties of the **Co₄-POM**.

Electrocatalytic OER evaluation of the Co₄/Mg₂Al nanocomposites:

The electrocatalytic OER activity of the **Co₄/Mg₂Al** nanocomposites was evaluated with the aim of first, studying the effect of the **Co₄-POM** in the LDH compared with the water-insoluble **CsCo₄-POM** salt and **Co₃O₄**; second, determining the optimal amount the **Co₄-POM** to maximize the OER activity of the composite among the tested samples; third, to assess the influence of the working media and the nature of the catalytic species in the POM-based hybrid since hydrolysis of **Co₄-POM** may lead to $Co(II)_{aq}$ leached in a solution that forms self-assembled CoO_x species under working conditions acting as heterogeneous electrode-bound OER active species.[41,42] Hence, we have performed the OER experiments using three different electrolytes: (i) sodium phosphate (NaP_i) at pH 6.9; (ii) sodium borate (NaB_i) at pH 9; and (iii) potassium hydroxide at pH 14.2.

In this regard, linear sweep voltammetry was used to evaluate the OER electrocatalytic activity of the nanocomposites. Figure S7a shows the results obtained using the NaP_i buffer at pH 6.9. As expected, the **Mg₂Al-LDH** (catalyst-free, blank) does not display any OER activity. On the contrary, the **Co₄/Mg₂Al** nanocomposites exhibit an important OER activity, which increase with the amount of **Co₄-POM** intercalated, whereby only **Co₄/Mg₂Al_3** shows an improved OER activity compared to that of **CsCo₄-POM**. The reason for this small improvement resides in the total amount of **Co₄-POM** present in each electrode. Therefore, considering that all the samples share the same OER catalytic species, this result is not surprising since there is a larger quantity of POM per gram of sample in **CsCo₄-POM** than in **Co₄/Mg₂Al_3**. In order to allow for a fair comparison that permits us to study the intrinsic activity of each sample, we have normalized the obtained current densities per nmol of Co present in each electrode, although only two of the four Co atoms in the POM structure can act as active sites. Figure 3a demonstrates the superior OER performance of the **Co₄/Mg₂Al** nanocomposites, outperforming that of **CsCo₄-POM.** Therefore, we can unequivocally say that the efficiency of **Co₄-POM** has been substantially improved in our nanocomposites. Interestingly, we can also observe that the hybrid with the highest **Co₄-POM** loading does not yield the highest OER activity. This feature suggests that high POM loadings in the lamellar space of the LDH may preclude part of the active sites from being reached by water molecules resulting in a decrease of the efficiency. In our case, the **Co₄/Mg₂Al_2** sample leads to the highest OER efficiency. Furthermore, we have also compared the OER activity of the hybrids with that of Co_3O_4 under the same experimental conditions and considering the number of nmols of Co employed. The results clearly demonstrate that Co_3O_4 cannot attain the OER activity displayed by our **Co₄/Mg₂Al** nanocomposites.

The calculated overpotentials displayed by the **Co₄/Mg₂Al** nanocomposites decrease when increasing the **Co₄-POM** loadings into the LDH, reaching a minimum value of 548 mV in **Co₄/Mg₂Al_3**, which is 19 mV lower than that for **CsCo₄-POM** (See Table S2 and Figure S8). Additionally, analysis of the Tafel behavior displayed by the materials shows rather high Tafel slopes in all cases with values between 194 and 316 mV/dec (Figure 3d, Figure S7a and Table S2). The Tafel slope depends solely on the rate-determining step of the catalytic reaction independently of the quantity of active sites present in the material.[43] Hence, these high Tafel slopes indicate that the catalytic OER is limited by a diffusion process and electron transfer.[31] It is further striking that **CsCo₄-POM** typically displays a much lower Tafel slope in the range of 70–
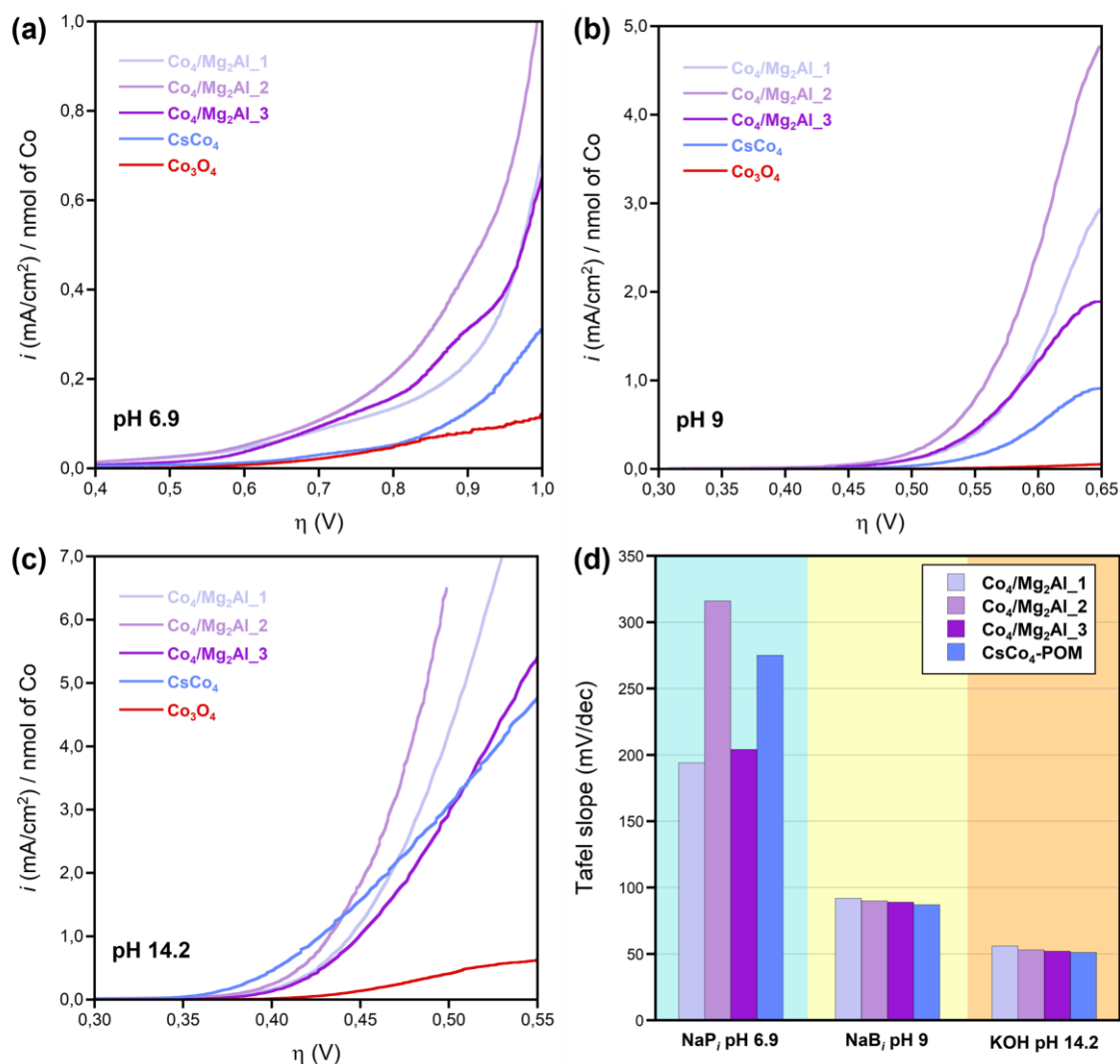
8

Figure 3: Electrocatalytic OER performance of the hybrid **Co₄/Mg₂Al** nanocomposites compared to that of **CsCo₄-POM** and of commercial Co_3O_4 considering the nmols of Co employed in each experiment performed in **a)** Sodium phosphate (0.1M) buffer with $NaNO_3$ (1M) at pH 6.9; **b)** Sodium borate (0.1M) buffer with $NaNO_3$ (1M) at pH 9; **c)** Potassium hydroxide (1M) at pH 14.2. **(d)** Calculated Tafel slopes of all the **Co₄-POM**-containing samples.

80 mV/dec as part of a modified carbon paste electrode.[18,44] This value contrasts with the Tafel slope of 275 mV/dec obtained for **CsCo₄-POM** in the present case. Hence, this result suggests that the observed high Tafel slope is originated, at least in part, by the use of a Nafion ink.

Following our study, we then performed the OER analysis using a NaB$_i$ buffer at pH 9. Under these working conditions, **Co₄/Mg₂Al_3**, **Co₄/Mg₂Al_2**, and **CsCo₄-POM** display similar OER activities and superior to that shown by **Co₄/Mg₂Al_1** (Figure S7b). Moreover, **Co₄/Mg₂Al_3** and **Co₄/Mg₂Al_2** show an overpotential of 452 mV, whereas the overpotential for **CsCo₄-POM** is 464 mV (Table S2 and Figure S8). The calculated Tafel slopes are close to 90 mV/dec, which are much closer to the expected values previously reported for **Co₄-POM** and indicate a rate-determining step limited by a competition between a chemical and an electron-transfer steps (Figure 3d, Figure S7b and Table S2). As previously observed, a comparison of the OER activity taking into account the nmols of Co employed in each electrode show the superior OER performance of the **Co₄/Mg₂Al** nanocomposites compared to that of **CsCo₄-POM**, with the **Co₄/Mg₂Al_2** hybrid showing again the best OER activity (Figure 3b). Additionally, comparison with the OER activity displayed by Co_3O_4 highlights the superior OER efficiency of our hybrid nanomaterials.

9

Finally, we analyzed the OER activity of the **Co₄/Mg₂Al** systems under strong alkali conditions using KOH at pH 14.2. It was previously reported that **Co₄-POM** in solution undergoes hydrolytic decomposition above pH 10 leading to the formation of the corresponding oxide species.[39] Nevertheless, Co-POMs can be stabilized by the proper selection of the environment in which they are dispersed to perform the electrocatalytic tests, for instance with the use of carbon paste.[11,45] Therefore, given the superior OER efficiency displayed by the nanocomposites compared to **CsCo₄-POM** and Co₃O₄, it seems reasonable to test our materials under basic conditions and analyze whether the **Mg₂Al-LDH** component is able to protect the **Co₄-POM** from hydrolytic decomposition.

Figure S7c shows a clear change in the OER behavior of the nanocomposites under basic conditions compared to the above-described results since none of them could perform a better catalytic activity than **CsCo₄-POM**. In fact, **Co₄/Mg₂Al_3**, **Co₄/Mg₂Al_2** display an overpotential of 370 mV, which is substantially higher than the value of 322 mV shown by **CsCo₄-POM** (Table S2 and Figure S8). Moreover, we can observe a change in the rate-determining step of the catalytic reaction limited by a chemical step, most likely the O-O bond formation. This is exemplified by the change in the Tafel slope with values between 51 and 56 mV/dec (Figure 3d, Figure S7c and Table S2). Additionally, the comparison of the results when considering the nmols of Co employed in each experiment also shows differences in the trends previously observed. In this case, **CsCo₄-POM** shows a better initial OER activity than the nanocomposites. However, when the applied overpotential reaches approximately 450 mV, **Co₄/Mg₂Al_1** and **Co₄/Mg₂Al_2** display better performances (Figure 3c). The origin of this change in the OER activity may be originated by a change in the reaction kinetics displayed by the materials that depend on the applied potential, i.e. a change in the Tafel behavior . This causes a decrease of the OER kinetics of **CsCo₄-POM** at high overpotentials that is more pronounced than that observed in the hybrids. Finally, even though the nanocomposites do not improve the OER activity of **CsCo₄-POM**, we can see that Co₃O₄ OER activity is much lower than those of **Co₄-POM** containing samples.

It is important to note that under these strong alkali conditions, we could observe the appearance of a redox event during the preconditioning CV cycles of the **Co₄/Mg₂Al** nanocomposites centered at 0.29 V (Figure S9). This redox event can be attributed to the Co(II)/Co(III) redox pair due to the Co leaching from the **Co₄-POM** framework, which would indicate that the **Mg₂Al-LDH** does not possess the ability to stabilize the **Co₄-POM**. This feature, together with the change in the OER activity trend observed made us ponder whether the **Co₄-POM** is the true active species or, on the contrary, hydrolytic decomposition of the POM under strong alkali media leads to the formation of the corresponding OER catalytically active CoOₓ species during electrocatalytic working conditions.

Stability of the Co₄/Mg₂Al nanocomposites:

To unravel the pH-dependent stability of the nanocomposites we have performed a battery of ex-situ and in-situ tests employing the **Co₄/Mg₂Al_3** hybrid since it contains the highest amount of **Co₄-POM**, thus it will aid in the evaluation of the fate of the catalyst.

We first analyzed the stability of **Co₄/Mg₂Al_3** by simply immersing the material in the three buffer solutions under stirring for 72 hours. Thereafter, the hybrid was recovered, washed, and dried in air. Powder X-ray diffraction patterns of the recovered **Co₄/Mg₂Al_3** show that the
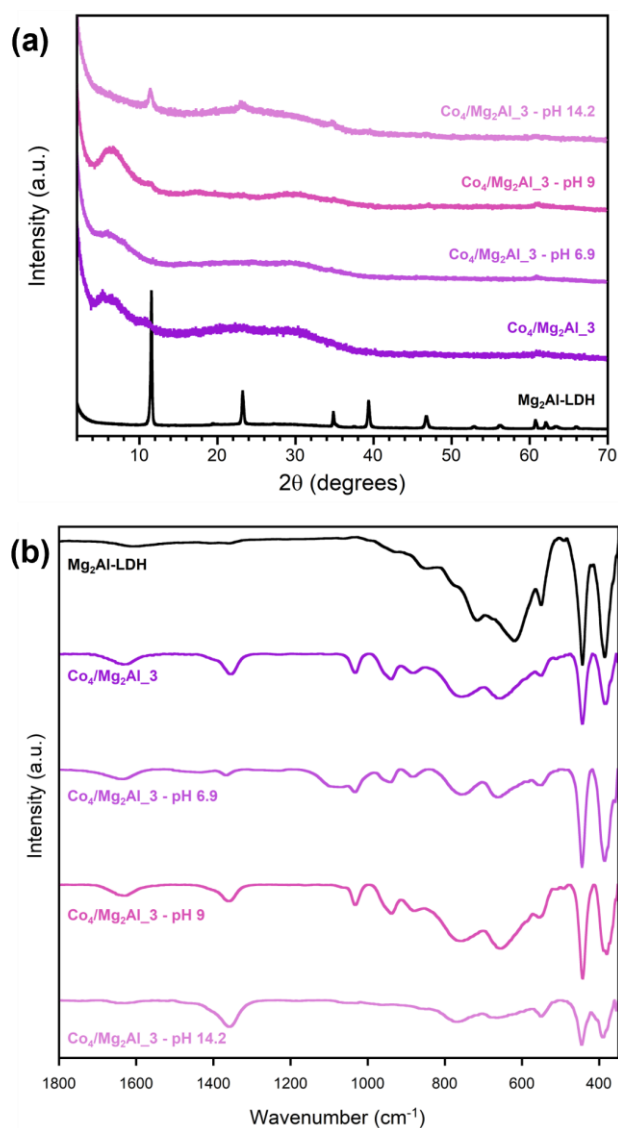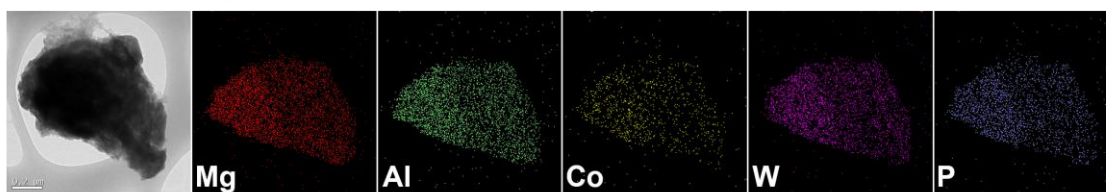
Figure 4: Powder X-ray diffraction patterns **(a)** and FT-IR spectra **(b)** of the **Co₄/Mg₂Al_3** nanocomposite collected after being dispersed in the different buffer solutions for 72 hours.

structure of **Co₄/Mg₂Al_3** is maintained at pH 6.9 and 9 (Figure 4a). However, an obvious change occurred at pH 14.2, in which the structure of the original **Mg₂Al-LDH** was recovered with no accountable sign of **Co₄-POM** present in the lamellar space of the LDH. Additionally, the FT-IR spectra seem to confirm this behavior since we could still observe the corresponding bands of **Co₄-POM** at pH 6.9 and 9, whereas they are not present at pH 14.2 (Figure 4b). Interestingly, we could observe an extra broad band around 1080 cm^{-1} in the recovered **Co₄/Mg₂Al_3** sample at pH 6.9 that is assigned to the intercalation of phosphates in the LDH that have been adsorbed from the NaP$_i$ buffer. In fact, this behavior is not surprising given the good phosphate adsorption properties of LDHs.[46] The morphology and composition of these samples were analyzed by TEM and EDX analysis (Figure 5 a-c). TEM images show that the platelet-like hexagonal crystallites are partially broken and assembled into bigger aggregates, whereas EDX mapping indicates that the **Co₄-POM** is retained in the nanocomposites at 6.9 and 9. However, at pH 14.2 the **Co₄-POM** is clearly unstable as confirmed by the enormous decrease of W and P content from the hybrids. In other words, at pH 6.9 and 9 the W:Co:P ratios are maintained with respect to the freshly made **Co₄-POM**, whereas the concentration of Co is one order of magnitude higher than that of W and P when the sample was immersed in KOH at pH 14.2 (see Table 1), clearly indicating the hydrolytic decomposition of **Co₄-POM**. This hydrolytic decomposition is further supported by XPS data. High-resolution XPS of the component elements clearly shows the substantial loss of W and P atoms from the hybrid, but the Co atoms seem to remain in the lamellar space of **Mg₂Al-LDH** appearing as Co(II) ions. In addition to this, the O1s XPS spectrum shows a decrease in the deconvoluted peak at 530.69 eV assigned to M-O terminal oxygens of the **Co₄-POM** framework.

11

(a) Hybrid **Co$_4$/Mg$_2$Al_3** nanocomposite recovered from the NaP$_i$ buffer at pH 6.9

(b) Hybrid **Co$_4$/Mg$_2$Al_3** nanocomposite recovered from the NaB$_i$ buffer at pH 9
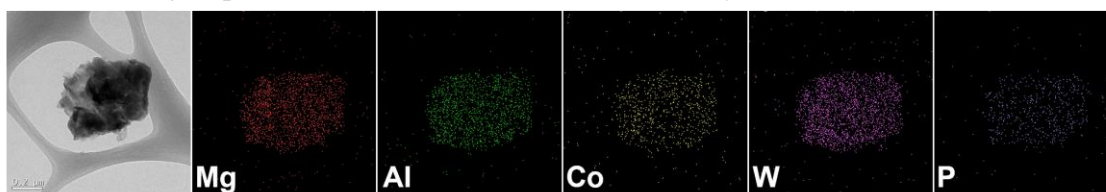
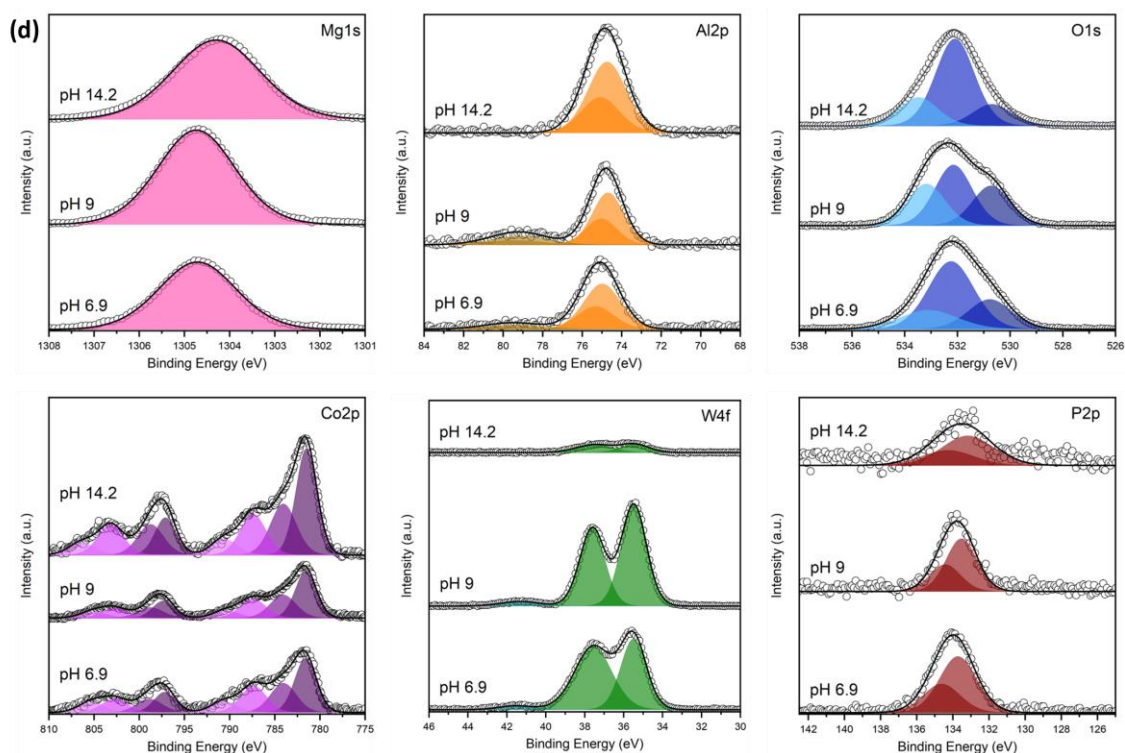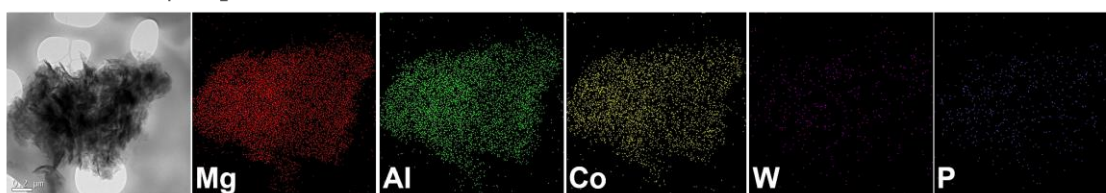**(c)** Hybrid **Co$_4$/Mg$_2$Al_3** nanocomposite recovered from the KOH solution at pH 14.2

Figure 5: TEM images and EDX mapping **(a-c)** and XPS data **(d)** of the hybrid **Co$_4$/Mg$_2$Al_3** nanocomposite collected after being dispersed in the different buffer solutions for 72 hours.

12

Table 1: Molar ratio extracted from the elemental analysis (EDX) performed on the recovered **Co₄/Mg₂Al_3** samples after being in suspension in the buffers for 72 hours.

Molar ratio	Expected	Co₄/Mg₂Al_3 NaP$_i$ pH 6.9	Co₄/Mg₂Al_3 NaB$_i$ pH 9	Co₄/Mg₂Al_3 NaOH pH 14.2
Mg:Al	2:1	2.00:1.34	2.00:1.10	2.00:0.93
W:Co:P	18:4:2	18.00:4.19:9.95*	18.00:4.57:1.96	18.00:167.14:11.57

*The high quantity of phosphorous found in this sample arises from the adsorption of phosphates from the NaP$_i$ buffer solution by the LDH counterpart.

The ex-situ characterization already provides strong evidence that **Co₄-POM** may be stable at close-to-neutral pH values but suffers from hydrolytic decomposition in strong basic conditions. The remaining question is whether they suffer the same fate under OER working conditions. For this reason, we conducted long-term stability tests by performing chronoamperometry measurements at the three different pH values studied above. For these experiments, we employed fluorine-doped tin oxide (FTO) working electrodes to foster a more facile post-catalytic characterization of the **Co₄/Mg₂Al_3** nanocomposite directly on the surface of the electrode, since the recovery of the catalyst from the Nafion ink is a challenging task and may result in the transformation or complete loss of the OER active material during the process. Unfortunately, these measurements did not deliver stable current densities, since the constant evolution of oxygen gas bubbles would damage the deposited ink resulting in the partial detachment and loss of the material from the surface of the electrode. Nevertheless, we could still perform in-situ XPS measurements of the material that remained attached on the surface of the FTOs electrodes after the 24 hours of chronoamperometry measurements (Figure 6). In this case, we observe a decrease of the typical satellite peaks of Co(II), which indicate a partial Co oxidation leading to a mixture of Co(II)/(III), especially at pH 9 and 14.2. Again, the loss of W and P atoms at pH 14.2 also occurs under working conditions and, to our surprise, we can also see the partial loss of P atoms at pH 9, as suggested by the decrease in the relative intensities of such elements with respect to the rest of the elements present in the same measured sample. This may indicate a partial hydrolytic decomposition of **Co₄-POM** at pH 9, whereby different **Co₄-POM** related species may be present in the lamellar space of the **Mg₂Al-LDH**. This feature can also be seen in the O1s XPS spectra in which the deconvoluted peak assigned to the terminal oxygens of the POM framework (W=O) has shifted at pH 9 to lower binding energies with respect to the experiment performed at pH 6.9, whereas it is completely absent at pH 14.2. In addition, we identified further differences with respect to the ex-situ XPS measurements regarding the stability of **Mg₂Al-LDH**. Therefore, under OER working conditions at pH 14.2, the high resolution Al2p XPS edge shows a decrease in the overall quantity of Al atoms present in the nanocomposite, whereas the O1s XPS can only be deconvoluted in one broad peak centered at 532.54 eV that can be assigned to Al(OH)$_x$ species formed from the Al(III) ions leached from the LDH structure.[47] This indicates that even being synthesized in basic media, the stability of the LDH under harsh oxidizing conditions may not be sufficient in the long term.
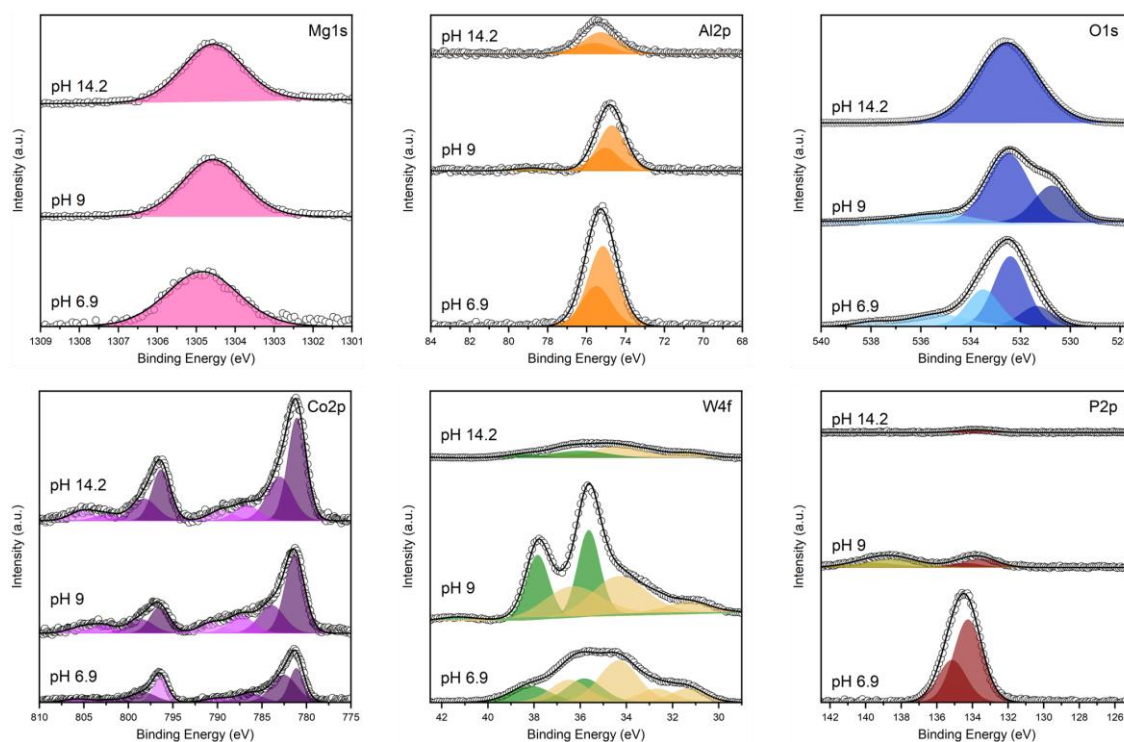
13

Figure 6: Post-catalytic XPS data of the recovered Nafion inks containing the hybrid **Co₄/Mg₂Al_3** nanocomposite after 24 hours of chronoamperometric measurements. Note that the Valence region of the Nafion polymer shows a strong overlap with the W4f edge (see Figure S10). These fitted bands are shown in yellow in the W4f data plot.

CONCLUSIONS

In this work, we have employed three different methods for the intercalation of **Co₄-POM** in the lamellar space of the **Mg₂Al-LDH**, which resulted in the fabrication of three **Co₄/Mg₂Al** nanocomposites with different amounts of **Co₄-POM**. Characterization of the hybrids confirmed the successful intercalation of the POM and allowed us to quantify the amount of **Co₄-POM** present in each sample. Thereafter, we studied the electrocatalytic OER activity of the **Co₄/Mg₂Al** nanocomposites employing different buffer solutions, from neutral pH to alkali media. We observe that the **Co₄/Mg₂Al_2** sample performs an overall better OER activity than the other samples tested when considering the number of mols of **Co₄-POM** present in each hybrid. Interestingly, **Co₄/Mg₂Al_2** does not contain the highest amount of **Co₄-POM** among the three studied samples, which indicates that higher loadings of the POM do not benefit the OER activity, possibly due to the decrease of channels in the lamellar space of the LDH from which water has to penetrate to reach the POM. Additionally, comparison with the parent, water-insoluble cesium salt of the POM (**CsCo₄-POM**), and with Co_3O_4 demonstrates the superior OER efficiency of the **Co₄/Mg₂Al** nanocomposites per mol of Co atom. This improvement has been attributed to better dispersion of the POM over the surface of a 2D material such as the LDH, hence thus increasing the number of active sites (i.e. Co-OH₂ sites) readily accessible for the water molecules. It is also interesting to mention that using formamide to obtain the swollen phase of the LDH delivers the **Co₄/Mg₂Al_3** nanocomposite with the highest amount of intercalated **Co₄-POM**; still, this sample does not show the highest OER efficiency. As mentioned before, the **Co₄/Mg₂Al_2** nanocomposite, for which water was employed to obtain the swollen phase of the LDH, shows the highest OER efficiency amongst the samples tested in this work. Therefore, we provide with an environmentally friendly method for the fabrication and optimization of POM/LDH nanocomposites with high catalytic efficiencies without the use of organic solvents

14

and easily oxidizable organic ligands, such as the Tris ligand. Interestingly, this method can be extrapolated to a variety of catalytic reactions beyond the energy production area.

In the quest to study the fate of the **Co₄-POM** OER catalyst under working environment that can aid in the understanding of the present POM/LDH nanocomposite, and other systems reported by other groups, we have performed a battery of ex-situ and in-situ characterization techniques. Our results indicate that **Co₄-POM** is stable in neutral media, but the POM structure is completely lost in strong alkali media. In the later, the W and P ions that compose the POM framework are almost completely expelled from the lamellar space of the LDH leading to Co(II) ions intercalated in the LDH. Interestingly, these Co ions can be partially oxidized under an applied potential and possibly form a layered mixed-valence Co oxide. This is an intriguing behavior that could open a new avenue for the fabrication of van der Waals heterostructures formed by alternating layers of different metal oxides and with interest to the wider research community. The instability issues shown by the intercalated **Co₄-POM** in strong alkali media are in fact not surprising since it was already demonstrated that this POM suffers from hydrolytic stability at pH values higher than 10. Moreover, we could also identify a decrease of the Al content in the LDH in strong basic conditions that can compromise the stability of the hybrids. Finally, the scenario at pH 9 does not seem to be trivial and further synchrotron-based characterization techniques are envisioned to accurately assess the observed behavior. In this case, ex-situ characterization agrees well with the intercalated **Co₄-POM** being stable; however, in-situ XPS data suggests a partial decomposition of the POM, whereby **Co₄-POM** and related species may coexist in the lamellar space of the LDH.

Our results demonstrate that the Keggin framework of the **Co₄-POM** intercalated in the lamellar space of an LDH suffers from hydrolytic stability issues when the pH value of the solution surpasses the pH window of stability of the POM in aqueous solution. This behavior can be extended to other polyoxotungstates and polyoxomolybdates that have been employed for the fabrication of similar hybrid systems towards water splitting. Therefore, we would like to emphasize that a careful study of the stability of the materials under working conditions is of utmost importance to accurately assess the OER activity, to identify the fate of the catalysts and, if so, to identify the true OER active species.

AUTHOR CONTRIBUTIONS

J.S.-L. conceived the project and carried out the syntheses, chemical characterization, and electrochemical measurements together with J.Q.-H. A.S.-D.S. assisted in the synthesis and characterization of the LDHs under the supervision of G.A.; R.T.-C. analyzed the XPS data; E.A.-G. performed and analyzed the adsorption/desorption measurements; J.S.-L. prepared the manuscript; all authors contributed to discussions throughout the project and the final editing of the manuscript.

CONFLICT OF INTEREST

G. Abellán is founder of Matteco.

ACKNOWLEDGEMENTS

REFERENCES

(1) Galán-Mascarós, J. R. Photoelectrochemical solar fuels from carbon dioxide, water and sunlight. *Catal. Sci. Technol.* 2020; **10**: 1967–1974. https://doi.org/10.1039/C9CY02606A.

(2) Eisenberg, R.; Gray, H. B.; Crabtree, G. W. Addressing the challenge of carbon-free energy. *Proc. Natl. Acad. Sci. U.S.A.* 2020, **117:** 12543–12549. https://doi.org/10.1073/pnas.1821674116.

(3) van der Spek, M.; Banet, C.; Bauer, C.; Gabrielli, P.; Goldthorpe, W.; Mazzotti, M.; Munkejord, S. T.; Røkke, N. A.; Shah, N.; Sunny, N.; Sutter, D.; Trusler, J. M.; Gazzani, M. Perspective on the hydrogen economy as a pathway to reach net-zero CO_2 emissions in Europe. *Energy Environ. Sc.i* 2022, **15**: 1034–1077. https://doi.org/10.1039/D1EE02118D.

(4) McKone, J. R.; Lewis, N. S.; Gray, H. B. Will solar-driven water-splitting devices see the light of day? *Chem. Mater.* 2014, **26**: 407–414. https://doi.org/10.1021/cm4021518.

(5) Craig, M. J.; Coulter, G.; Dolan, E.; Soriano-López, J.; Mates-Torres, E.; Schmitt, W.; García-Melchor, M. Universal scaling relations for the rational design of molecular water oxidation catalysts with near-zero overpotential. *Nat. Commun.* 2019, **10**: 4993. https://doi.org/10.1038/s41467-019-12994-w.

(6) McCrory, C. C. L.; Jung, S.; Ferrer, I. M.; Chatman, S. M.; Peters, J. C.; Jaramillo, T. F. Benchmarking hydrogen evolving reaction and oxygen evolving reaction electrocatalysts for solar water splitting devices. *J. Am. Chem. Soc.* 2015, **137**: 4347–4357. https://doi.org/10.1021/ja510442p.

(7) Roger, I.; Shipman, M. A.; Symes, M. D. Earth-abundant catalysts for electrochemical and photoelectrochemical water splitting. *Nat. Rev. Chem.* 2017, **1**: 0003. https://doi.org/10.1038/s41570-016-0003.

(8) Gao, D.; Trentin, I.; Schwiedrzik, L.; González, L.; Streb, C. The reactivity and stability of polyoxometalate water oxidation electrocatalysts. *Molecules* 2020, **25**: 1–20. https://doi.org/10.3390/molecules25010157.

(9) Vickers, J. W.; Lv, H.; Sumliner, J. M.; Zhu, G.; Luo, Z.; Musaev, D. G.; Geletii, Y. V; Hill, C. L. Differentiating homogeneous and heterogeneous water oxidation catalysis: Confirmation that $[Co_4(H_2O)_2(\alpha\text{-}PW_9O_{34})_2]^{10-}$ is a molecular water oxidation catalyst. *J Am Chem Soc* **2013**, *135* (38), 14110–14118. https://doi.org/10.1021/ja4024868.

(10) Natali, M.; Bazzan, I.; Goberna-Ferrón, S.; Al-Oweini, R.; Ibrahim, M.; Bassil, B. S.; Dau, H.; Scandola, F.; Galán-Mascarós, J. R.; Kortz, U.; Sartorel, A.; Zaharieva, I.; Bonchio, M. Photo-assisted water oxidation by high-nuclearity cobalt-oxo cores:

Tracing the catalyst fate during oxygen evolution turnover. *Green Chem.* 2017, **19**: 2416–2426. https://doi.org/10.1039/C7GC00052A.

(11)   Blasco-Ahicart, M.; Soriano-López, J.; Carbó, J. J.; Poblet, J. M.; Galán-Mascarós, J. R. Polyoxometalate electrocatalysts based on earth-abundant metals for efficient water oxidation in acidic media. *Nat. Chem.* 2018, **10**: 24–30. https://doi.org/10.1038/nchem.2874.

(12)   Lv, H.; Song, J.; Geletii, Y. V.; Vickers, J. W.; Sumliner, J. M.; Musaev, D. G.; Kögerler, P.; Zhuk, P. F.; Bacsa, J.; Zhu, G.; Hill, C. L. An exceptionally fast homogeneous carbon-free cobalt-based water oxidation catalyst. *J. Am. Chem. Soc.* 2014, **136**: 9268–9271. https://doi.org/10.1021/ja5045488.

(13)   Soriano-López, J.; Musaev, D. G.; Hill, C. L.; Galán-Mascarós, J. R.; Carbó, J. J.; Poblet, J. M. Tetracobalt-polyoxometalate catalysts for water oxidation: Key mechanistic details. *J. Catal.* 2017, ***350***: 56–63. https://doi.org/10.1016/j.jcat.2017.03.018.

(14)   Soriano-López, J.; Song, F.; Patzke, G. R.; Galán-Mascarós, J. R. Photoinduced Oxygen Evolution Catalysis Promoted by Polyoxometalate Salts of Cationic Photosensitizers. *Front. Chem.* 2018, **6**: 302. https://doi.org/10.3389/fchem.2018.00302.

(15)   Martin-Sabi, M.; Soriano-López, J.; Winter, R. S.; Chen, J.-J.; Vilà-Nadal, L.; Long, D.-L.; Galán-Mascarós, J. R.; Cronin, L. Redox tuning the Weakley-type polyoxometalate archetype for the oxygen evolution reaction. *Nat. Catal.* 2018, **1**: 208–213. https://doi.org/10.1038/s41929-018-0037-1.

(16)   Haider, A.; Bassil, B. S.; Soriano-López, J.; Qasim, H. M.; Sáenz de Pipaón, C.; Ibrahim, M.; Dutta, D.; Koo, Y.-S.; Carbó, J. J.; Poblet, J. M.; Galán-Mascarós, J. R.; Kortz, U. 9-Cobalt(ii)-containing 27-tungsto-3-germanate(IV): Synthesis, structure, computational modeling, and heterogeneous water oxidation catalysis. *Inorg. Chem.* 2019, **58**: 11308–11316. https://doi.org/10.1021/acs.inorgchem.9b01495.

(17)   Tao, M.; Yin, Q.; Kaledin, A. L.; Uhlikova, N.; Lu, X.; Cheng, T.; Chen, Y.-S.; Lian, T.; Geletii, Y. V.; Musaev, D. G.; Bacsa, J.; Hill, C. L. Structurally Precise Two-Transition-Metal Water Oxidation Catalysts: Quantifying adjacent 3d metals by synchrotron X-radiation anomalous dispersion scattering. *Inorg. Chem.* 2022, **61**: 6252–6262. https://doi.org/10.1021/acs.inorgchem.2c00446.

(18)   Soriano-López, J.; Steuber, F. W.; Mulahmetović, M.; Besora, M.; Clemente-Juan, J. M.; O'Doherty, M.; Zhu, N.-Y.; Hill, C. L.; Coronado, E.; Poblet, J. M.; Schmitt, W. Accelerating water oxidation – A mixed Co/Fe polyoxometalate with improved turnover characteristics. *Chem. Sci.* 2023, **14**: 13722–13733. https://doi.org/10.1039/D3SC04002J.

(19)   Cherevan, A. S.; Nandan, S. P.; Roger, I.; Liu, R.; Streb, C.; Eder, D. Polyoxometalates on functional substrates: Concepts, synergies, and future perspectives. *Adv. Sci.* 2020, **7**: 1903511. https://doi.org/10.1002/advs.201903511.

(20)   Wu, J.; Liao, L.; Yan, W.; Xue, Y.; Sun, Y.; Yan, X.; Chen, Y.; Xie, Y. Polyoxometalates immobilized in ordered mesoporous carbon nitride as highly efficient water

oxidation catalysts. *ChemSusChem* 2012, **5**: 1207–1212. https://doi.org/10.1002/cssc.201100809.

(21) Mukhopadhyay, S.; Debgupta, J.; Singh, C.; Kar, A.; Das, S. K. A Keggin polyoxometalate shows water oxidation activity at neutral pH: POM@ZIF-8, an efficient and robust electrocatalyst. *Angew. Chem.* Int. Ed. 2018, **57**: 1918–1923. https://doi.org/10.1002/anie.201711920.

(22) Li, T.; Miras, H. N.; Song, Y. F. Polyoxometalate (POM)-Layered double hydroxides (LDH) composite materials: Design and catalytic applications. *Catalysts*. 2017, **7**: 260. https://doi.org/10.3390/catal7090260.

(23) Stamate; Pavel; Zavoianu; Marcu. Highlights on the catalytic properties of polyoxometalate-intercalated layered double hydroxides: A review. *Catalysts* 2020, 10: 57. https://doi.org/10.3390/catal10010057.

(24) Ullah, I.; Munir, A.; Haider, A.; Ullah, N.; Hussain, I. Supported polyoxometalates as emerging nanohybrid materials for photochemical and photoelectrochemical water splitting. *Nanophotonics* 2021, **10**: 1595–1620. https://doi.org/10.1515/nanoph-2020-0542.

(25) Proust, A.; Matt, B.; Villanneau, R.; Guillemot, G.; Gouzerh, P.; Izzet, G. Functionalization and Post-Functionalization: A step towards polyoxometalate-based materials. *Chem. Soc. Rev.* 2012, **41**: 7605. https://doi.org/10.1039/c2cs35119f.

(26) Liu, K.; Yao, Z.; Song, Y.-F. Polyoxometalates hosted in layered double hydroxides: Highly enhanced catalytic activity and selectivity in sulfoxidation of sulfides. *Ind. Eng. Chem. Res.* 2015, **54**: 9133–9141. https://doi.org/10.1021/acs.iecr.5b02298.

(27) Liu, K.; Xu, Y.; Yao, Z.; Miras, H. N.; Song, Y. Polyoxometalate-intercalated layered double hydroxides as efficient and recyclable bifunctional catalysts for cascade reactions. *ChemCatChem* 2016, **8**: 929–937. https://doi.org/10.1002/cctc.201501365.

(28) Xue, X.; Yu, F.; Li, J.-G.; Bai, G.; Yuan, H.; Hou, J.; Peng, B.; Chen, L.; Yuen, M.-F.; Wang, G.; Wang, F.; Wang, C. Polyoxometalate intercalated NiFe layered double hydroxides for advanced water oxidation. *Int. J. Hydrogen Energy* 2020, **45**: 1802–1809. https://doi.org/10.1016/j.ijhydene.2019.11.038.

(29) Gumerova, N. I.; Rompel, A. Polyoxometalates in solution: Speciation under spotlight. *Chem. Soc. Rev.* 2020, **49**: 7568–7601. https://doi.org/10.1039/D0CS00392A.

(30) Yu, L.; Liang, Q. A fully noble-metal-free electrocatalyst based on a cobalt-polyoxometalate immobilized in a layered double hydroxide for water oxidation at neutral pH. *New J. Chem.*2022, **46**: 3073–3077. https://doi.org/10.1039/D1NJ05630A.

(31) Soriano-López, J.; Elliott, R.; Kathalikkattil, A. C.; Ako, A. M.; Mulahmetović, M.; Venkatesan, M.; Schmitt, W. Bioinspired water oxidation using a Mn-oxo cluster stabilized by non-innocent organic tyrosine Y161 and plastoquinone mimics. *ACS*

Sustain. Chem. Eng. 2020, **8**: 13648–13659. https://doi.org/10.1021/acssuschemeng.0c03379.

(32) Soriano-López, J.; Elliott, R.; Kathalikkattil, A. C.; Ako, A. M.; Schmitt, W. Tuning the catalytic water oxidation activity through structural modifications of high-nuclearity Mn-oxo clusters [Mn$_{18}$M] (M = Sr^{2+}, Mn^{2+}). *Water* 2021, **13**: 2042. https://doi.org/10.3390/w13152042.

(33) Gautam, J.; Wang, P.; Chishti, A. N.; Ma, Z.; Liu, Y.; Jiang, X.; Zha, J.; Zhang, L.-N.; Diao, G.; Wei, Y.; Ni, L. Heterointerface engineering of hierarchically assembling polyoxometalate on zinc/iron layered double hydroxide nanosheet as a remarkable bifunctional electrocatalyst for overall water splitting. *J. Power Sources* 2023, **581**: 233502. https://doi.org/10.1016/j.jpowsour.2023.233502.

(34) Pettersson, L.; Andersson, I.; Oehman, L. O. Multicomponent polyanions. 39. Speciation in the aqueous hydrogen ion-molybdate(MoO42-)-hydrogenphosphate(HPO$_4$$^{2-}$) system as deduced from a combined emf-phosphorus-31 NMR study. *Inorg. Chem.* 1986, **25**: 4726–4733. https://doi.org/10.1021/ic00246a028.

(35) Briand, L. E.; Valle, G. M.; Thomas, H. J. Stability of the phospho-molybdic Dawson-type ion P$_2$Mo$_{18}$O$_{62}$$^{6-}$ in aqueous media. *J. Mater. Chem.* 2002, **12**: 299–304. https://doi.org/10.1039/b106769a.

(36) Okamoto, K.; Iyi, N.; Sasaki, T. Factors affecting the crystal size of the MgAl-LDH (layered double hydroxide) prepared by using ammonia-releasing reagents. *Appl. Clay Sci.* 2007, **37**: 23–31. https://doi.org/10.1016/j.clay.2006.10.008.

(37) Liu, Z.; Ma, R.; Osada, M.; Iyi, N.; Ebina, Y.; Takada, K.; Sasaki, T. Synthesis, anion exchange, and delamination of Co–Al layered double hydroxide: Assembly of the exfoliated nanosheet/polyanion composite films and magneto-optical studies. *J. Am. Chem. Soc.* 2006, **128**: 4872–4880. https://doi.org/10.1021/ja0584471.

(38) Newman, S. P.; Jones, W. Synthesis, characterization and applications of layered double hydroxides containing organic guests. *New J. Chem.* 1998, **22:** 105–115. https://doi.org/10.1039/a708319j.

(39) Goberna-Ferrón, S.; Soriano-López, J.; Galán-Mascarós, J. R.; Nyman, M. Solution speciation and stability of cobalt-polyoxometalate water oxidation catalysts by X-ray scattering. *Eur. J. Inorg. Chem.* 2015, **2015**: 2833–2840. https://doi.org/10.1002/ejic.201500404.

(40) Theiss, F. L.; Ayoko, G. A.; Frost, R. L. Thermogravimetric analysis of selected layered double hydroxides. *J. Therm. Anal. Calorim.* 2013, **112**: 649–657. https://doi.org/10.1007/s10973-012-2584-z.

(41) Stracke, J. J.; Finke, R. G. Distinguishing homogeneous from heterogeneous water oxidation catalysis when beginning with polyoxometalates. *ACS Catal.* 2014, **4**: 909–933. https://doi.org/10.1021/cs4011716.

(42) Folkman, S. J.; Soriano-Lopez, J.; Galán-Mascarós, J. R.; Finke, R. G. Electrochemically driven water-oxidation catalysis beginning with six exemplary cobalt polyoxometalates: Is it molecular, homogeneous catalysis or electrode-

bound, heterogeneous CoO$_x$ catalysis? *J. Am. Chem. Soc.* 2018, **140**: 12040–12055. https://doi.org/10.1021/jacs.8b06303.

(43) Kushner-Lenhoff, M. N.; Blakemore, J. D.; Schley, N. D.; Crabtree, R. H.; Brudvig, G. W. Effects of aqueous buffers on electrocatalytic water oxidation with an iridium oxide material electrodeposited in thin layers from an organometallic precursor. *Dalton Trans.* 2013, **42**: 3617. https://doi.org/10.1039/c2dt32326e.

(44) Azmani, K.; Besora, M.; Soriano-López, J.; Landolsi, M.; Teillout, A.-L.; de Oliveira, P.; Mbomekallé, I.-M.; Poblet, J. M.; Galán-Mascarós, J.-R. Understanding polyoxometalates as water oxidation catalysts through iron vs. cobalt reactivity. *Chem. Sci.* 2021, **12**: 8755–8766. https://doi.org/10.1039/D1SC01016F.

(45) Arens, J. T.; Blasco-Ahicart, M.; Azmani, K.; Soriano-López, J.; García-Eguizábal, A.; Poblet, J. M.; Galán-Mascarós, J. R. water oxidation electrocatalysis in acidic media with Co-containing polyoxometalates. *J. Catal.* 2020, **389:** 345–351. https://doi.org/10.1016/j.jcat.2020.06.006.

(46) Keyikoglu, R.; Khataee, A.; Yoon, Y. Layered double hydroxides for removing and recovering phosphate: Recent advances and future directions. *Adv. Colloid. Interface Sci.* 2022, **300:** 102598. https://doi.org/10.1016/j.cis.2021.102598.

(47) Seijas-Da Silva, A.; Sanchis-Gual, R.; Carrasco, J. A.; Oestreicher, V.; Abellán, G.; Coronado, E. Boosting the supercapacitive behavior of CoAl layered double hydroxides via tuning the metal composition and interlayer space. *Batteries & Supercaps* 2020, **3**: 499–509. https://doi.org/10.1002/batt.201900223.

Supplementary Information

Elucidation of the activity and pH stability limits of polyoxometalate-intercalated layered double hydroxide nanocomposites towards water oxidation catalysis

Joaquín Soriano-López,[a]* Javier Quirós-Huerta,[a] Álvaro Seijas-Da Silva,[a] Ramón Torres-Cavanillas,[a] Eduardo Andres-Garcia,[a] Gonzalo Abellán[a] and Eugenio Coronado[a]

[a]Institut de Ciència Molecular, Universitat de València, Catedrático José Beltrán 2, 46980 Paterna, Spain

*Correspondence to: joaquin.soriano@uv.es

Table of contents

1) Instrumentation and Methodology:

Attenuated Total Reflectance Fourier-Transform Infrared (ATR-FTIR): Spectra were collected using an Agilent Cary 630 FTIR spectrometer in the 4000–350 cm^{-1} range.

Inductively Coupled-Plasma Mass Spectrometry (ICP-MS): The ICP-MS analyses were performed at the University of Valencia (Sección de Espectrometría Atómica y Molecular). The samples were digested in acid medium at 220°C using a microwave oven.

Transmission Electron Microscopy and Electron Diffraction X-ray Scattering (TEM and EDX): TEM images and EDX mapping were performed in a HRTEM TECNAI 200 kV microscope operating at 200 kV. The samples were prepared by dropping sample suspension in EtOH on lacey formvar/carbon copper grids (330 mesh).

Powder X-Ray Diffraction (PXRD): PXRD patterns were collected using a capillary with a PANalytical X'Pert diffractometer at room temperature using the copper radiation (Cu-Kα = 1.54178 Å) in the 2-70 degrees region.

Textural characterization: Adsorption/desorption volumetric isotherms were carried out in a Tristar II Plus Micromeritics sorptometer, for CO_2 (at 273 K, 1 bar). Sample activation was performed at 373 K, under vacuum overnight.

Thermogravimetric Differential Thermal Analysis (TG-DTA): TG-DTA data was acquired in air using a Mettler Toledo TGA/SDTA 851e model in the 25–700°C temperature range with a temperature ramp of 10°C/min.

Thermogravimetric Analysis (TGA): TGA of **KCo$_4$-POM** was carried out under N_2 atmosphere employing a TA instruments TGA 550 in the 25–700°C temperature range with a temperature ramp of 5°C/min.

X-ray Photoelectron Spectroscopy (XPS): XPS measurements were performed in an ultrahigh vacuum system ESCALAB210 (base pressure 1.0×10^{-10} mbar) from Thermo VG Scientific. Photoelectrons were excited by using the Mg Kα line (1253.6 eV). All spectra were referred to the Fermi level.

2) Materials and Synthetic Details:

All chemical reagents were used as purchased without further purification. Sodium tungstate dihydrate, sodium phosphate dibasic, sodium phosphate monobasic monohydrate, boric acid, potassium acetate, sodium chloride, sodium nitrate, cesium chloride, magnesium chloride hexahydrate, urea, hydrochloric acid, and Nafion™ 117 solution (~5%) were purchased from Sigma-Aldrich. Cobalt acetate tetrahydrate and carbon black, acetylene 50% compressed were purchased from Alfa Aesar. Aluminum chloride hexahydrate, glacial acetic acid, and potassium hydroxide (99.99%) were purchased from Thermo Scientific Chemicals. Ethanol absolute and isopropanol were purchased from Scharlab. Milli-Q water was obtained from a Millipore Milli-Q equipment.

Synthesis of K$_{10}$[Co$_4$(H$_2$O)$_2$(B-α-PW$_9$O$_{34}$)$_2$]·44.2H$_2$O (Co$_4$-POM): This well-known polyoxometalate was prepared applying an optimized literature method.[1] Na$_2$WO$_4$·2H$_2$O (33.0 g, 100 mmol) and Na$_2$HPO$_4$ (1.57 g, 11.1 mmol) were dissolved in 100 mL of H$_2$O and the pH was adjusted to 6.5 through addition of glacial acetic acid. Then, a solution containing Co(CH$_3$COO)$_2$·4H$_2$O (5.48 g, 22 mmol) dissolved in 50 mL of H$_2$O was added to this mixture. The resulting dark-purple solution was refluxed for 2 hours. Thereafter, the mixture was filtered twice to remove a residual purple precipitate. The resulting solution was saturated with 3 g of potassium acetate, filtered again, and allowed to cool at room

temperature. Rhombic, purple crystals of **Co₄-POM** were collected by filtration, washed with water, methanol, and acetone. The sample was dried in air.

The compound was characterized by FT-IR (Figure S1), POM composition was calculated by elemental analysis (ICP-MS) (Table S1), and water content was calculated by thermogravimetric analysis (TGA) (weight loss: 13.46%). Mw = 5918.04 g/mol

Preparation of $Cs_{8.3}K_{1.7}[Co_4(H_2O)_2(B-\alpha-PW_9O_{34})_2]\cdot14H_2O$ (CsCo₄-POM): CsCo₄-POM was achieved by metathesis reaction following an established literature method[2] and characterized by FT-IR (Figure S1) and by elemental analysis (ICP-MS)
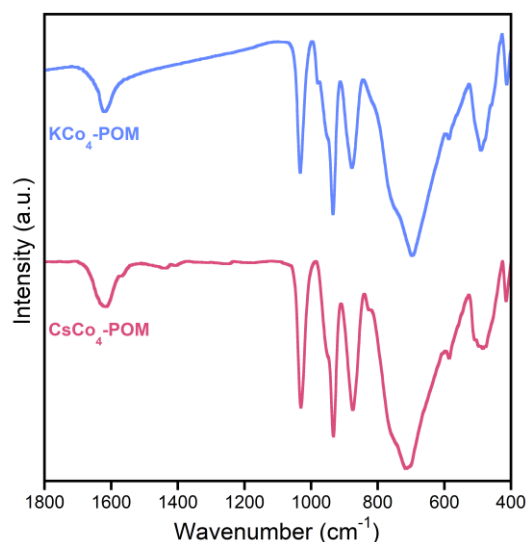

Figure S1: FT-IR spectra of **KCo₄-POM** and **CsCo₄-POM**.

Synthesis of Mg₂Al-Cl-LDH (Mg₂Al-LDH): This LDH was prepared by the urea hydrolysis method under hydrothermal conditions. In a first step, 250 mM aqueous solutions of $MgCl_2\cdot6H_2O$ and $AlCl_3\cdot6H_2O$ were prepared separately employing milliQ H_2O and stored at 4°C. Then, 36 mL of the $MgCl_2$ solution and 18 mL of the $AlCl_3$ solution were mixed in a Teflon vial, and the final volume was increased to 90 mL with the addition of 36 mL of milliQ H_2O. To this solution, 2.365 g (39.4 mmols) of urea were added and the resulting mixture was stirred for 5 minutes. The Teflon vial was placed in the autoclave and the reaction was carried out in an oven at 140°C for 24 hours. After cooling down to room temperature, the obtained **Mg₂Al-LDH** was recovered by centrifugation, washed with milliQ H_2O until the resulting washing waters had a neutral pH, then it was washed with EtOH, and dried under vacuum for 24 hours. Infra-red spectrum of the as-synthesized **Mg₂Al-LDH** indicates that in addition to chloride, carbonate anions have been also incorporated into the LDH interlayer space. The carbonate was removed from the structure by anion exchange. For this, we prepared first in a round bottom flask a 1M NaCl aqueous solution using 1 L of milliQ H_2O to which HCl was added until a final concentration of 3.3 mM Then, the solution was degassed with N_2. Thereafter, 1 g of the as-synthesized **Mg₂Al-Co₃-LDH** was dispersed in the aqueous solution, the round bottom flask was sealed, the suspension was stirred for 12 hours under a flow of N_2. This step was repeated twice to completely exchange the carbonate by chloride anions. Finally, the **Mg₂Al-Cl-LDH** was recovered by centrifugation, washed three times with milliQ H_2O, then with EtOH, and dried under vacuum overnight.
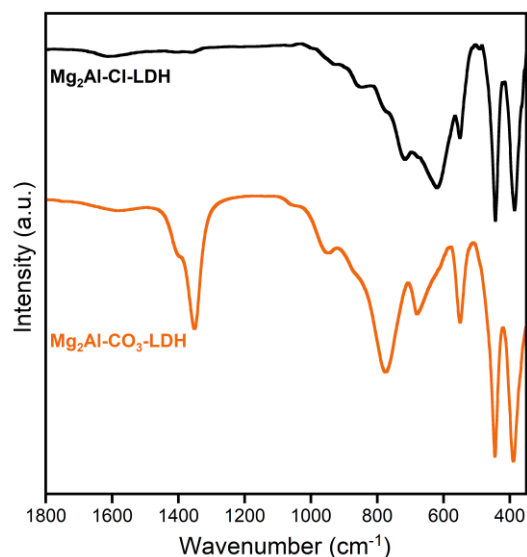
S3

Figure S2: FT-IR spectra of **Mg$_2$Al-Cl-LDH** and **Mg$_2$Al-CO$_3$-LDH**.

Fabrication of the hybrid Co$_4$/Mg$_2$Al nanocomposites:

*Preparation of **Co$_4$/Mg$_2$Al_1***: A 5 mM **Co$_4$-POM** aqueous solution was prepared by dissolving 148.5 mg of **Co$_4$-POM** in 5 mL of milliQ H$_2$O. The solution was then filtered using Nylon syringe filter, transferred into a vial, and degassed with Ar for 20 minutes. Then, 10 mg of **Mg$_2$Al-LDH** were added and the vial was sealed and sonicated for 20 minutes. After this, the solution was stirred while Ar was passed through the gas space of the vial using a syringe for 42 hours. Finally, the hybrid nanocomposite was collected by centrifugation, washed three times with milliQ H$_2$O, then with EtOH, and dried under vacuum overnight.

*Preparation of **Co$_4$/Mg$_2$Al_2***: A 5 mM **Co$_4$-POM** aqueous solution was prepared by dissolving 148.5 mg of **Co$_4$-POM** in 5 mL of milliQ H$_2$O. The solution was then filtered using Nylon syringe filter, transferred into a vial, and degassed with Ar for 20 minutes. Then, 10 mg of **Mg$_2$Al-LDH** were added and the vial was sealed and sonicated for 60 minutes. After this, the solution was stirred while Ar was passed through the gas space of the vial using a syringe for 42 hours. Finally, the hybrid nanocomposite was collected by centrifugation, washed three times with milliQ H$_2$O, then with EtOH, and dried under vacuum overnight.

*Preparation of **Co$_4$/Mg$_2$Al_3***: 8.0 mg of **Mg$_2$Al-LDH** were placed in a vial to which 4 mL of formamide were added. Then the vial was sealed and purged with Ar for 30 minutes and then, placed in the ultrasound bath for 20 minutes. Separately, 118.8 mg of **Co$_4$-POM** were dissolved in 4 mL of milliQ H$_2$O to obtain a 5 mM solution, which was also purged with Ar for 30 minutes. Thereafter, the **Co$_4$-POM** solution was added dropwise to the dispersed **Mg$_2$Al-LDH** and under stirring piercing a syringe through the septum of the sealed vial. After the complete addition of the **Co$_4$-POM** solution, Ar was passed through the gas space of the vial and left under stirring for 20 hours. Finally, the hybrid nanocomposite was collected by centrifugation, washed three times with milliQ H$_2$O, then with EtOH, and dried under vacuum overnight.

3) Electrochemical procedures:

The electrochemical measurements were performed in a typical three-electrode set-up using either a glassy carbon rotating disk electrode (RDE-GC, 0.07 cm^2) for cyclic voltammetry (CV) and linear sweep voltammetry (LSV) or a fluorine-dope tin oxide (FTO, 0.25 cm^2) for chronoamperometry as working electrode. The set-up was completed by a Ag/AgCl (3M KCl) double junction reference electrode and a Pt foil as counter electrode. Three different buffered solutions were employed in this work: i) sodium phosphate (0.1M) buffer at pH 6.9 with NaNO$_3$ (1M) as electrolyte (NaP$_i$); ii) sodium borate (0.1M) buffer at pH 9 with NaNO$_3$ (1M) as electrolyte (NaB$_i$); and iii) KOH (1M) at pH 14.2. Cyclic voltammetries and linear sweep voltammetries were performed using an Autolab PGSTAT 128N potentiostat/galvanostat. Chronoamperometric measurements were carried out in a Gamry 1000E potentiostat/galvanostat. The uncompensated resistance value was calculated using the utility implemented in the Gamry 1000E potentiostat/galvanostat prior to each LSV measurement by applying a constant OER overpotential of 300 mV. Ohmic drop (iR) of the LSV curves were then compensated (100%) during the data treatment using the formula: $E_{real} = E_{app} - iR$. Prior to each experiment, the buffer solutions were degassed with Ar for at least 30 minutes. Before conducting the LSV measurements, CV at a scan rate of 100 mV/s was performed as a preconditioning step of the materials until no substantial changes were observed (typically 20 cycles). LSVs were performed at a scan rate of 1 mV/s and at a rotation of 1600 rpm, which was controlled with an Autolab RDE motor controller. LSV data was used for Tafel analyses. Chronoamperometry measurements were carried out in an H-cell where the working and reference electrodes were separated from the counter electrode by a glass frit (P0). For these experiments the applied overpotentials were 700 mV, 600 mV, and 500 mV when using NaP$_i$ at pH 6.9, NaB$_i$ at pH 9, and KOH at pH 14.2, respectively. All the measurements were repeated at least three times to ensure reproducibility of the results.

The Nernst equation was employed to calculate the thermodynamic potential for the water oxidation ($E^0_{H_2O/O_2}$) at each pH used:

$$E^0_{H_2O/O_2} = 1.229 - (0.059 \times pH)(V) \text{ vs NHE at 25 °C} \qquad \text{(Eq. S1)}$$

All applied potentials (E_{app}) were converted to the NHE reference scale using $E_{NHE} = E_{Ag/AgCl} + 0.210$ (V). The overpotentials were calculated by subtracting the thermodynamic water oxidation potential ($E^0_{H_2O/O_2}$) from E_{app} as:

$$\eta = E_{app} - E^0_{H_2O/O_2} \qquad \text{(Eq. S2)}$$

The current densities were calculated based on the geometrical surface area of the electrodes. The obtained current densities were set of a value of 0 mA/cm^2 at 0 mV of overpotential to remove any possible contribution of capacitance to the electrocatalytic current. The onset potentials were estimated from the intersection point between the tangent lines of the Faradaic current at 0.2 mA/cm^2 and the non-Faradic current. Herein all the potentials are given versus NHE, unless otherwise stated.

Electrode preparation: Nafion inks were prepared by dispersing 2mg of each sample and 1 mg of carbon black in 0.5 mL of a 1:1 (H$_2$O:EtOH) solution and 10 µL of a Nafion™ 117 solution (~5%). Then the mixture was sonicated for 2 hours to obtain a homogeneous suspension. Aliquots of 5 µL were drop-casted on the glassy carbon electrodes (already polished with 1.0 and 0.05 µm alumina powder) and dried at room temperature, whereas aliquots of 20 µL were drop-casted on the FTO electrodes (washed by sequentially sonicating them in water and then in isopropanol for 3 minutes each, and dried with a nitrogen flow) and dried at 60 °C.
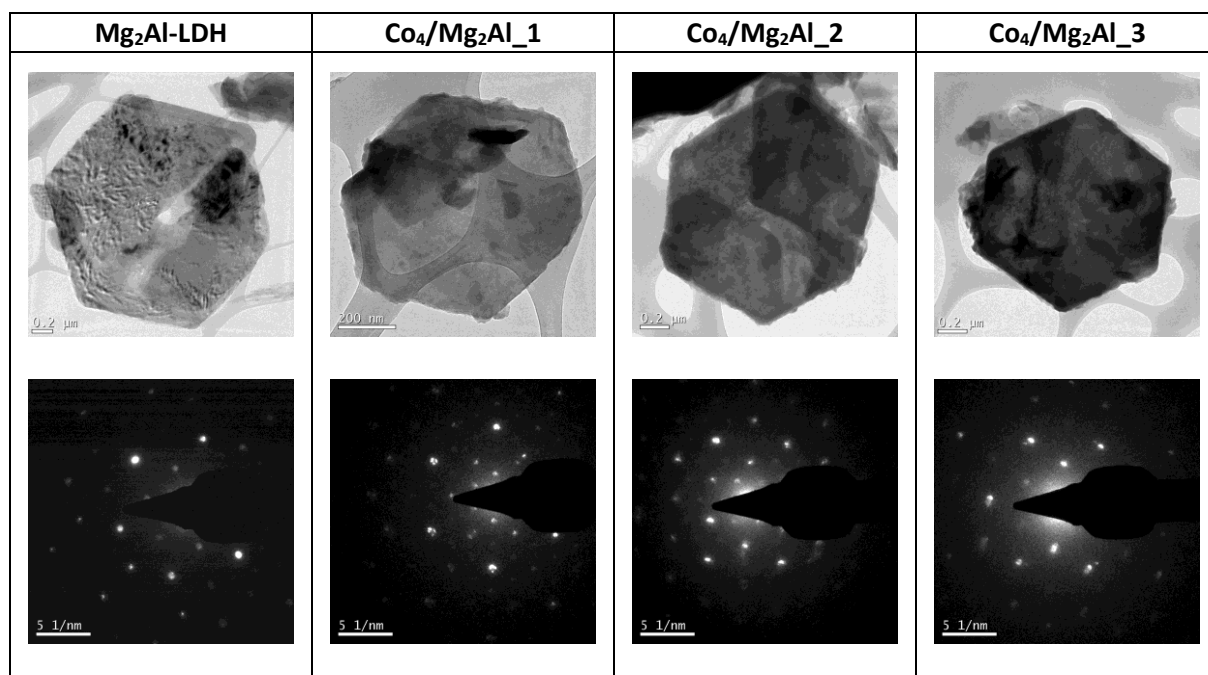
4) Characterization:

Mg₂Al-LDH	Co₄/Mg₂Al_1	Co₄/Mg₂Al_2	Co₄/Mg₂Al_3

Figure S3: TEM images and electron diffraction patterns of the **Mg₂Al-LDH** and the hybrid **Co₄/Mg₂Al** nanocomposites.
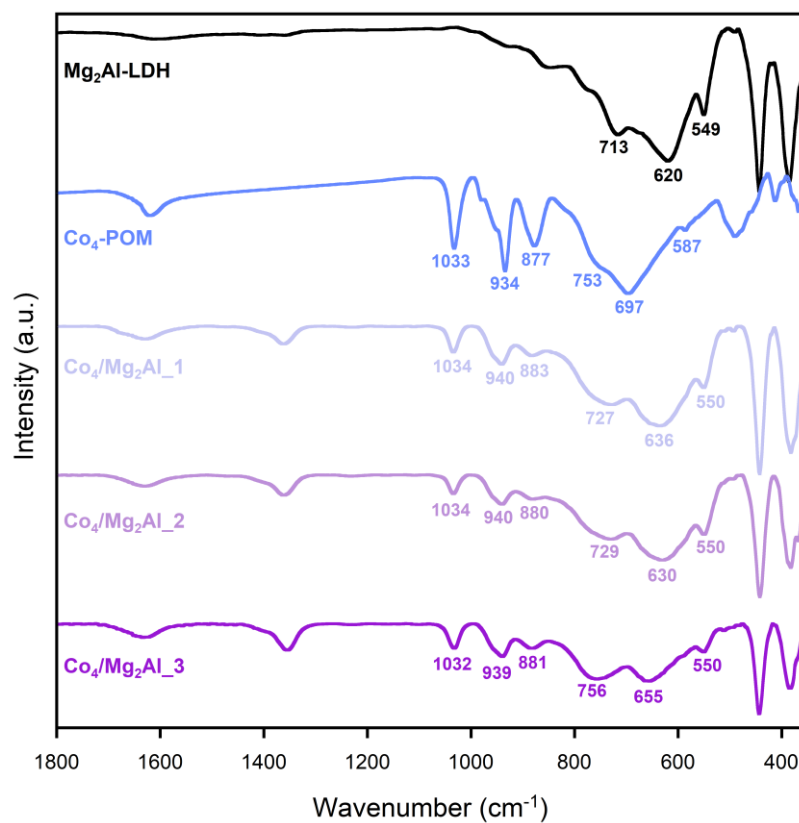

Figure S4: FT-IR spectra of the **Mg₂Al-LDH**, the **Co₄-POM**, and the hybrid **Co₄/Mg₂Al** nanocomposites.

S6

Table S2: Elemental analysis (ICP-MS) of the fresh samples. For those containing the **Co₄-POM** the data was normalized to the W content to facilitate the comparison. For **Mg₂Al-LDH** the data was normalized to the Mg content.

|		Mg	Al	Cl	Co	W	P
Mg₂Al-LDH	mg/g	215	123.9	12.5	-	-	-
	μmols/g	8845.92	4591.95	352.61	-	-	-
	molar ratio	2.00	1.04	0.079	-	-	-
Co₄/Mg2Al_1	mg/g	129.8	74.7	3.91	16.4	100.7	2.16
	μmols/g	5340.46	2768.51	110.30	278.28	547.76	69.74
	molar ratio	175.49	90.98	3.62	9.14	18.00	2.29
Co₄/Mg2Al_2	mg/g	88	48.7	8.6	12.39	115	2.41
	μmols/g	3620.65	1804.91	242.60	210.24	625.54	77.81
	molar ratio	104.18	51.94	6.98	6.05	18.00	2.24
Co₄/Mg2Al_3	mg/g	46.1	29.4	4.26	19.75	252.9	4.98
	μmols/g	1896.73	1089.62	120.17	335.13	1375.65	160.78
	molar ratio	24.82	14.26	1.57	4.39	18.00	2.10
KCo₄-POM	mg/g	-	-	-	43.5	492	10.24
	μmols/g	-	-	-	738.13	2676.24	330.6
	molar ratio	-	-	-	4.96	18.00	2.22
CsCo₄-POM	mg/g	-	-	-	40.6	539	8.98
	μmols/g	-	-	-	688.92	3013.49	289.92
	molar ratio	-	-	-	4.23	18.00	1.78
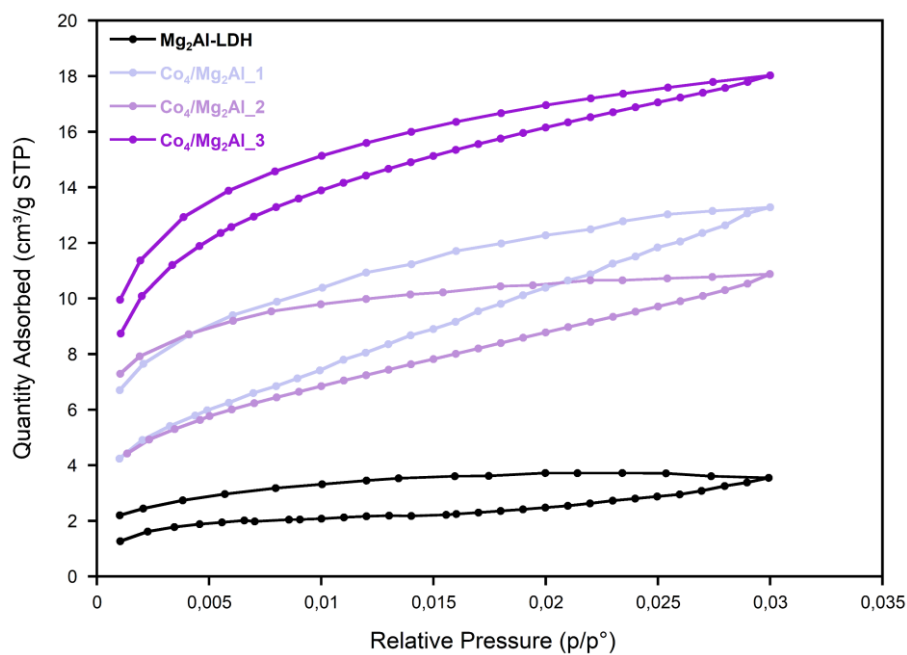
Figure S5: CO_2 adsorption/desorption isotherms of the **Mg₂Al-LDH** and the hybrid **Co₄/Mg₂Al** nanocomposites.
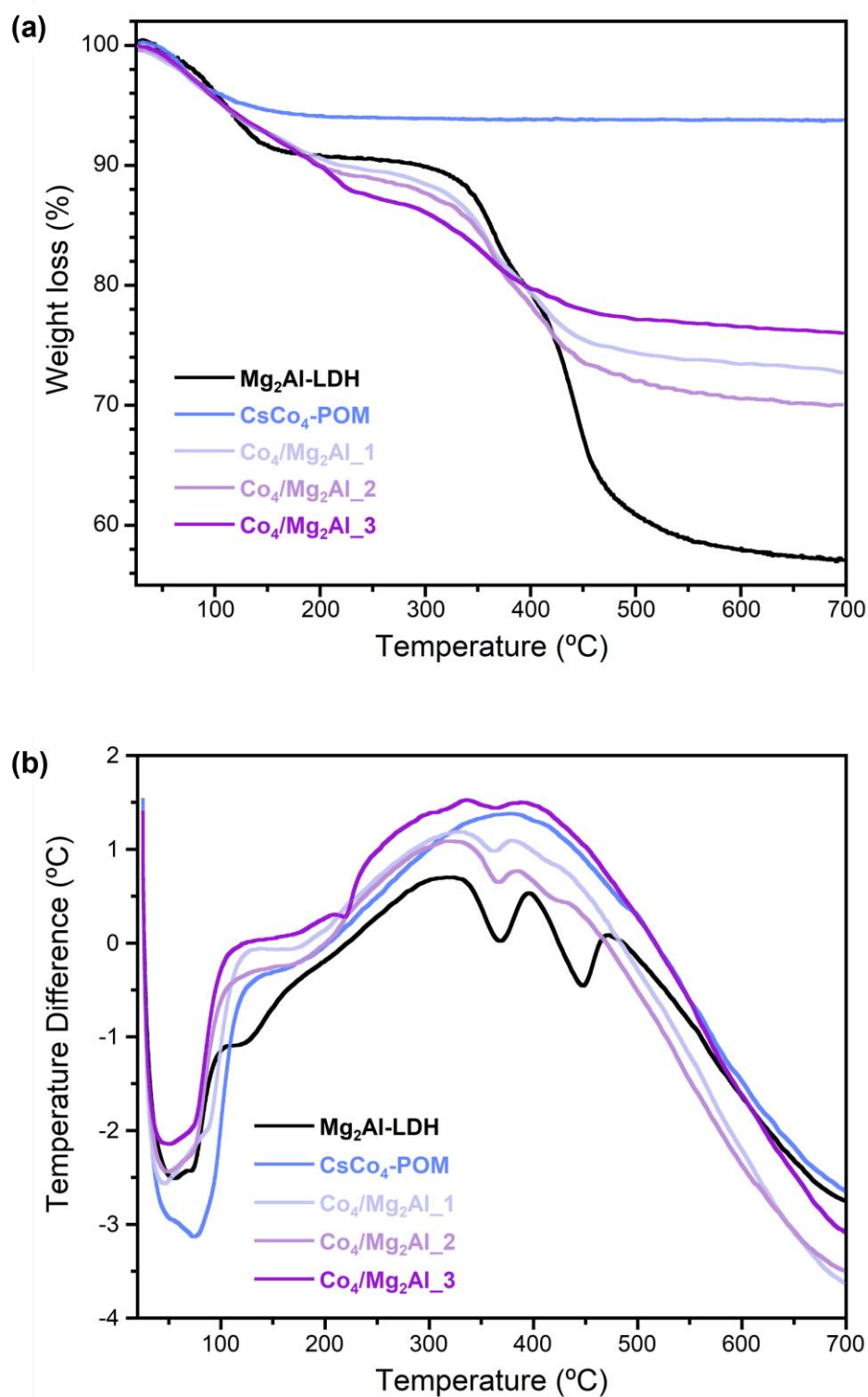
Figure S6: Thermogravimetric **(a)** and differential thermal analysis **(b)** of the **Mg₂Al-LDH**, the **CsCo₄-POM**, and the hybrid **Co₄/Mg₂Al** nanocomposites.
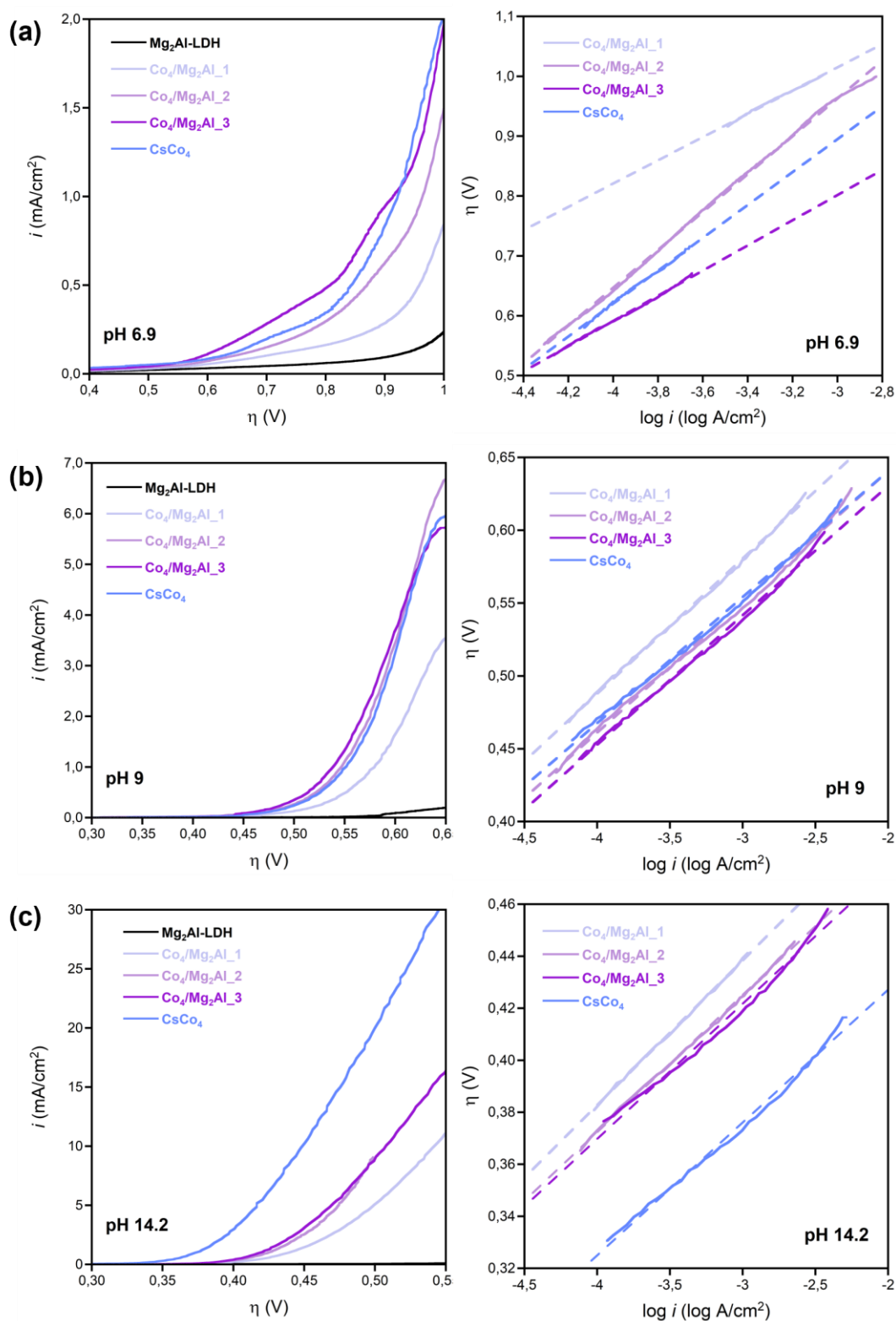
Figure S7: Linear sweep voltammetry (left) and Tafel plots (right) of the hybrid **Co₄/Mg₂Al** nanocomposites, **CsCo₄-POM**, and **Mg₂Al-LDH** performed in **a)** sodium phosphate (0.1M) buffer with NaNO₃ (1M) at pH 6.9; **b)** sodium borate (0.1M) buffer with NaNO₃ (1M) at pH 9; **c)** potassium hydroxide (1M) at pH 14.2.

Table S2: Calculated onset overpotentials and Tafel slopes of the different hybrid **Co₄/Mg₂Al** nanocomposites at the different working conditions compared to that of the **CsCo₄-POM**.

Sample	NaP$_i$ at pH 6.9		NaB$_i$ at pH 9		KOH at pH 14.2	
	η_{onset} (mV)	Tafel Slope (mV/dec)	η_{onset} (mV)	Tafel Slope (mV/dec)	η_{onset} (mV)	Tafel Slope (mV/dec)
Co₄/Mg₂Al_1	705	194	477	92	377	56
Co₄/Mg₂Al_2	584	316	452	90	370	53
Co₄/Mg₂Al_3	548	204	452	89	370	52
CsCo₄-POM	567	275	464	87	322	51

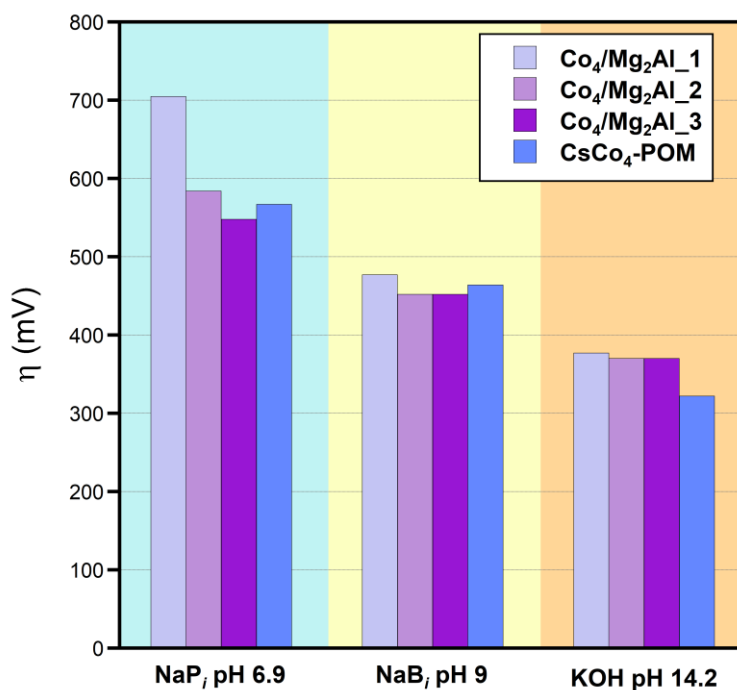**Figure S8:** Calculated onset overpotentials of the different hybrid **Co₄/Mg₂Al** nanocomposites at the different working conditions compared to that of the **CsCo₄-POM**.
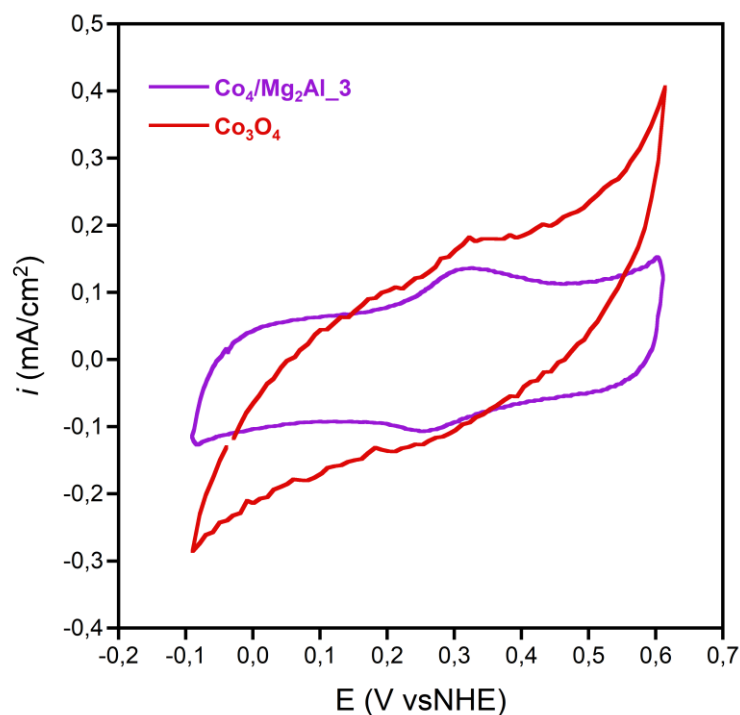
S10

Figure S9: Cyclic voltammogram showing the appearance of a redox peak in the hybrid **Co₄/Mg₂Al_3** nanocomposite during the preconditioning cycles performed in KOH (1M) at pH 14.2 compared to the preconditioning cycles of Co₃O₄. The redox event appears centered at 0.29 V and is assigned to the Co(II)/Co(III) pair originated from the Co(II) ions expelled from the **Co₄-POM** structure due to its hydrolytic decomposition under strong alkali media.
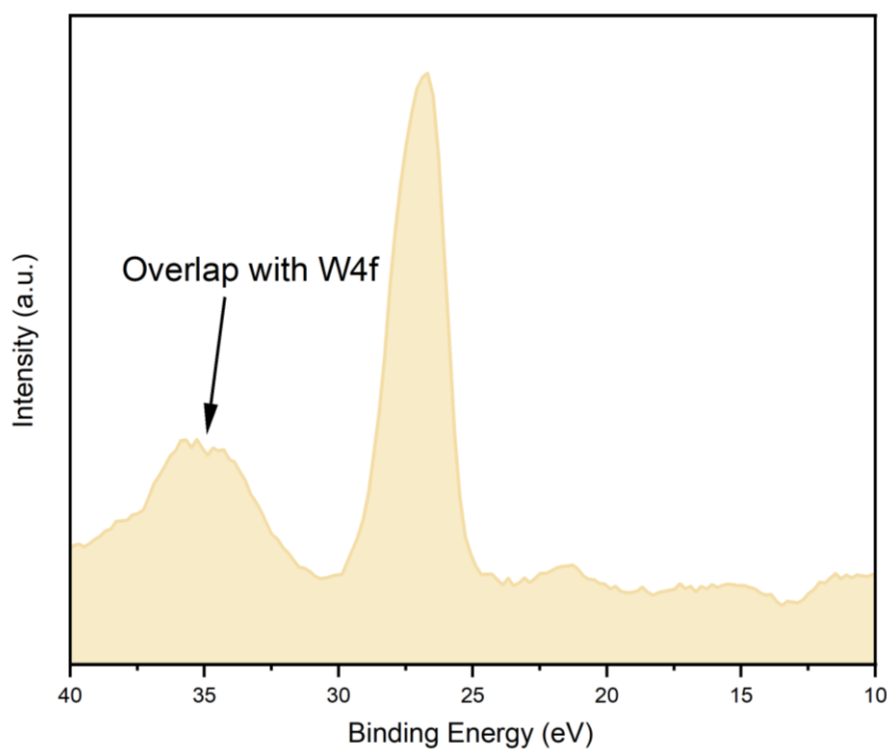

Figure S10: XPS valence region of a catalyst free Nafion ink showing the strong overlap with the W4f edge in the 30–40 eV region.

5) References:

(1)   Weakley, T. J. R.; Evans, H. T.; Showell, J. S.; Tourné, G. F.; Tourné, C. M. 18-
        Tungstotetracobalto(II)Diphosphate and Related Anions: A Novel Structural Class of
        Heteropolyanions. *J. Chem. Soc., Chem. Commun.* **1973**, No. 4, 139–140.
        https://doi.org/10.1039/C39730000139.

(2)   Arens, J. T.; Blasco-Ahicart, M.; Azmani, K.; Soriano-López, J.; García-Eguizábal, A.; Poblet, J.
        M.; Galan-Mascaros, J. R. Water Oxidation Electrocatalysis in Acidic Media with Co-Containing
        Polyoxometalates. *J Catal* **2020**, *389*, 345–351. https://doi.org/10.1016/j.jcat.2020.06.006.